IISc Theses Abstracts

Contents

J. Indian Inst. Sci., Nov.–Dec. 1996, 76, 851–903.

IISc THESES ABSTRACTS

Thesis Abstract (Ph. D.)

An experimental investigation of turbulent bursts in the atmospheric surface layer over the tropics by S. Rudra Kumar

Research supervisors: A. Prabhu and R. Narasimha

Department: Centre for Atmospheric Sciences

1. Introduction

Turbulence, an important characteristic of the atmospheric boundary layer (ABL), is mainly responsible for the transport of heat, moisture, momentum, pollutants, etc., in the atmosphere. As with any turbulent flow, our understanding of the ABL has to gain in large part from observational studies. So far several observational experiments have been carried out in the middle latitudes (*e.g.*, the famous Kansas and Minnesota experiments)[1], but similar experiments in the tropical regions, especially over land, have been rare. This work describes an observational study of the turbulent flow in the atmospheric surface layer of the Indian tropical region, and includes accounts of various stages in conducting the field experiments, the detailed quality checks made to validate the acquired data, and, finally, a description of the turbulent flow in terms of 'events', which has been considered in the recent past as possibly a more natural way of description.

2. The experiment and the data used

As part of the national experiment called MONTBLEX-90 (monsoon trough boundary layer experiment 1990), surface layer observations have been carried out using four 30 m instrumented towers, one each at Kharagpur, Varanasi, Jodhpur and Delhi, representing regions of deep moist convection, shallow dry convection and the transition between the two. Sensors for measuring both mean and fluctuating quantities of wind speed, temperature and humidity were used, with the majority of them indigenously built.

A block schematic of the tower instrumentation used is shown in Fig. 1. A pc-based data acquisition system built at our Centre, at the Indian Institute of Science, was used to acquire the fast response data, and an imported data logger for the mean data. There were six levels of sensors and instruments on the tower. The mean data was acquired round the clock while fluctuating quantities were acquired for 10–15 min every hour or once in three hours depending on whether or not there were any synoptic scale disturbances. A large set of data was acquired for a duration of about three months covering different stability conditions and different phases of the monsoon. Several checks[2] were made on randomly selected stretches of data to assess the quality of data.

3. Results from the study of turbulent bursts

Since the observations at Jodhpur were most successful in terms of number of good sets of continuous data, data from this site was selected for the investigation of events (or bursts) in the flow.

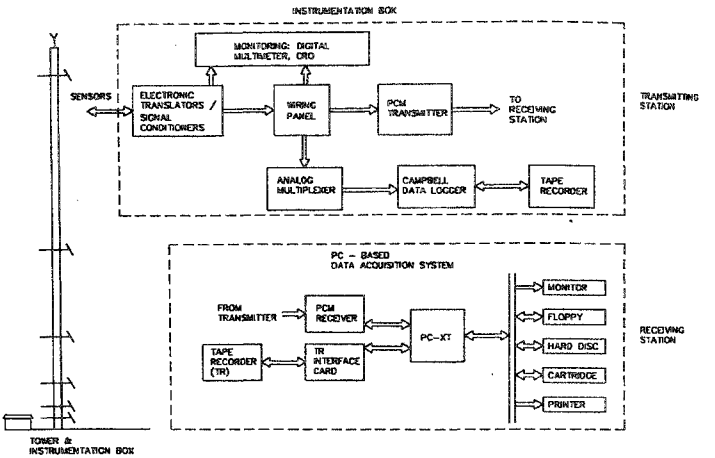

FIG. 1. Block schematic of a tower instrumentation system.

Employing the variable interval time averaging (VITA) technique[3] on the fluctuating components of horizontal streamwise velocity (u'), vertical velocity (w') and temperature (T') derived from sonic anemometer data, the burst characteristics in Jodhpur were compared with earlier work[4] on mid-latitude data (Boulder, USA), both taken under near-neutral stability conditions. Figure 2 shows a plot of event frequency *vs* threshold at two different averaging times for the

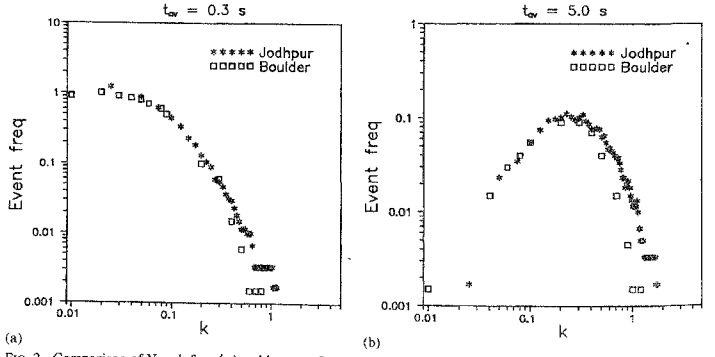

FIG. 2. Comparison of N *vs* k for u' signal between Jodhpur and Boulder: (a) $t_{av} = 0.3$s (b) $t_{av} = 5$s.

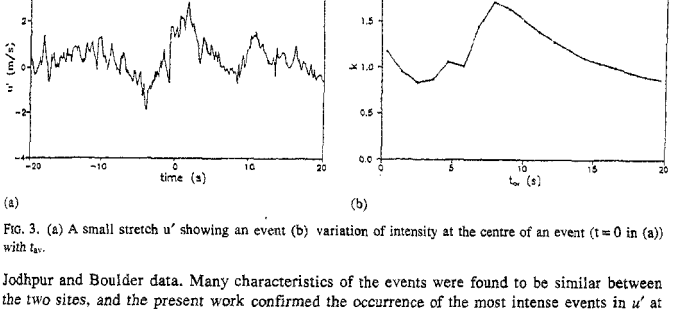

FIG. 3. (a) A small stretch u′ showing an event (b) variation of intensity at the centre of an event (t = 0 in (a)) *with* t_{av}.

Jodhpur and Boulder data. Many characteristics of the events were found to be similar between the two sites, and the present work confirmed the occurrence of the most intense events in u' at longer averaging times and those in w' at shorter averaging times.

In an attempt to identify the events with objectively determined intensity and duration parameters, we have improved the event-detection algorithm taking advantage of the scale-selective property of the VITA technique. As illustrated in Fig. 3, an event is tagged with a duration equal to an averaging time which results in maximum intensity. Using this modified algorithm we are able to draw a chronicle of events each with appropriate intensity and duration. Based on this chronicle, we have seen the characteristic signature of both accelerating and decelerating events which are found to be very similar to those found in earlier work in both laboratory and atmospheric flows. Figure 4 shows the characteristic signatures so determined, and also highlights (Fig 4(a)) the need to treat accelerating and decelerating events separately. Using three data sets under different stability conditions (neutral, stable and unstable), the conditional averages of w' and T' signals during eventful times for the u' signal are also determined.

Eventful periods in the flux signals are times during which there are significant deviations from the mean flux signal. The VITA technique tends to identify the front and back of such events as two separate events, and is in general misleading for describing flux events. However, a simple threshold technique turns out to be very effective. In this method, we first identify the times at which the instantaneous absolute value of the flux exceeds a prescribed threshold. Then the time interval between the nearest zero-crossing points on either side of each such cross-over is taken as the duration of the event and the midpoint of the interval as the centre of the event. The method is illustrated in Fig. 5.

Momentum and heat flux data are analysed based on this technique (using the rms value of the flux signal as the threshold), again for different stability conditions, and chronicles of events are drawn in each case. Here the events are divided into positive and negative depending on the sign of their contribution to the total flux. Based on such chronicles, the distribution of event durations and inter-arrival times is sketched, as is the ensemble average of events. Interestingly both positive and negative events when normalised appropriately show a Mexican hat-like structure as shown in Fig. 6 for the momentum flux events (a neutral case). The burstiness, a parameter introduced in an earlier study[4], when computed with the events detected from the present technique, is found to have much higher values (generally in excess of 0.75 for most of the data

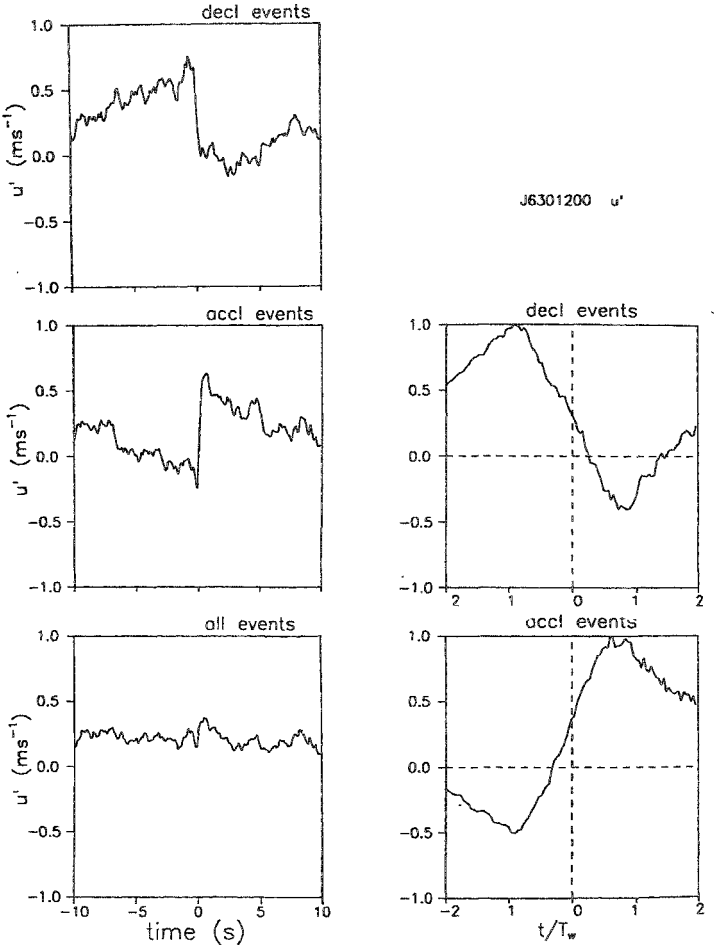

FIG. 4. Conditional average of u'-events: near-neutral case, (a) without normalisation, (b) normalised conditional average of accelerating and decelerating u'-events.

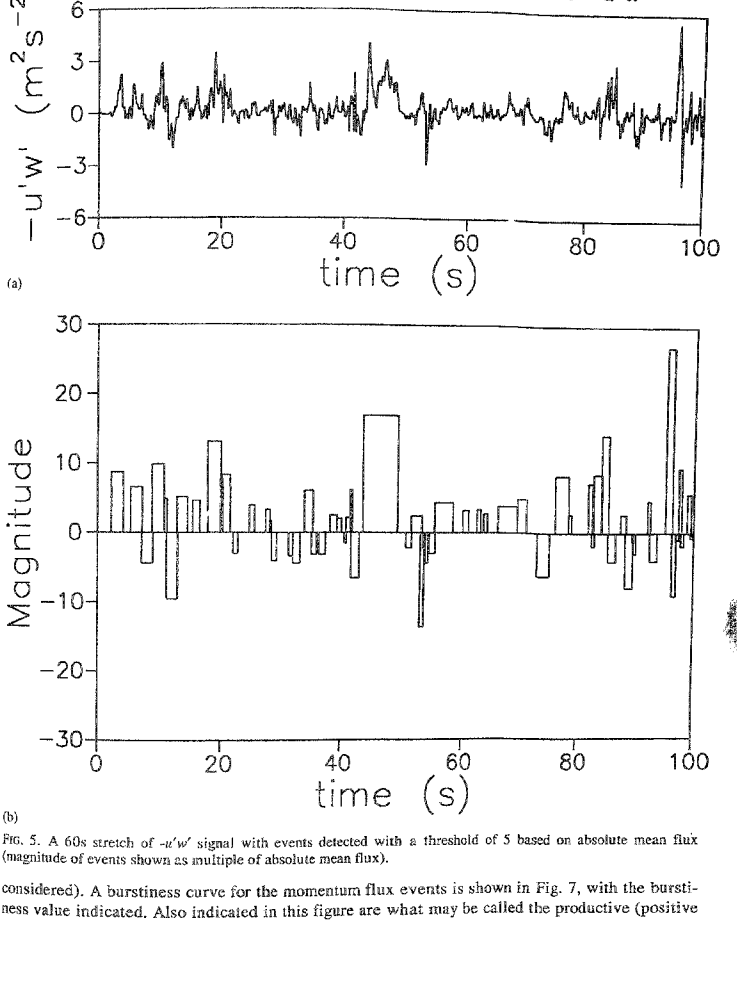

FIG. 5. A 60s stretch of $-u'w'$ signal with events detected with a threshold of 5 based on absolute mean flux (magnitude of events shown as multiple of absolute mean flux).

considered). A burstiness curve for the momentum flux events is shown in Fig. 7, with the burstiness value indicated. Also indicated in this figure are what may be called the productive (positive

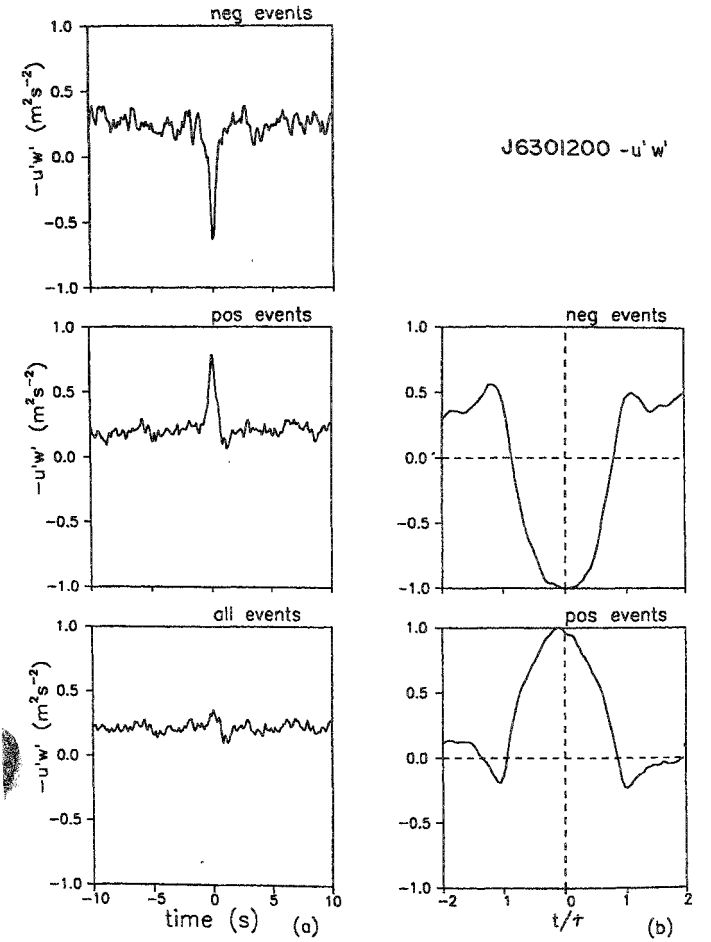

FIG. 6. (a) Simple conditional average of momentum flux events taking (i) all events, (ii) only positive events, and (iii) only negative events. (b) Normalised conditional average of positive and negative events.

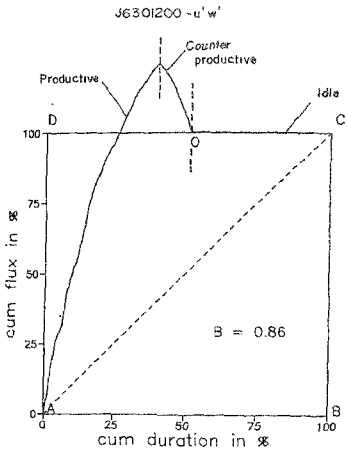

FIG. 7. Burstiness curve for $-u'w'$ events.

events), counter-productive (negative events) and idle (non-eventful) periods, which are, respectively, about 35, 15 and 50% of the total duration. Momentum flux events are found to have higher burstiness when compared to heat flux events. The simultaneous occurrence of momentum and heat flux events is examined by defining a coincidence coefficient, which is found to be very high (in the range 70–90%), suggesting that the turbulent fluid motions in the atmospheric surface layer responsible for momentum flux will most likely result in heat flux also.

4. Conclusions

The MONTBLEX-90 programme, carried out in different convective zones of the monsoon trough during 1990, has resulted in the acquisition of a valuable set of atmospheric data under varied stability conditions. The work reports the progress achieved in the major objective of describing turbulence in terms of events. A new procedure for constructing a chronicle of events is able to replace the given stretch of data by a series of 'events' tagging each of them with an appropriate duration and intensity (or magnitude).

A simple and effective method of detecting events in a flux signal has been suggested. Momentum and heat flux events so detected in general account for almost the entire flux, and occupy only about half the total time. The conditional averaging in flux events, with duration and amplitudes of events suitably normalised, results in something like a Mexican hat profile. The burstiness factor is generally found to be greater than 0.75 for most of the data considered, and the probability of simultaneous occurrence of momentum and heat flux events is very high (70–90%). From the diurnal variation of various event characteristics it is found that the dominance of positive (or negative) events changes clearly with time of day (or stability) in the case of heat flux events, while in the case of momentum flux positive events dominate during most of the day ex-

cept during periods of strong instability (namely in the afternoons), when negative events come close to positive events in all respects, occasionally even dominating them.

References

1. KAIMAL, J. C. AND WYNGAARD, J. C. The Kansas and Minnesota experiments. *Boundary Layer Meteorol.*, 1990, **50**, 31–47.
2. RUDRA KUMAR, S. AND PRABHU, A. Quality assessment of the tower data from MONTBLEX-90, Report 91MD3, Centre for Atmospheric Sciences, Indian Institute of Science, Bangalore.
3. BLACKWELDER, R. F. AND KAPLAN, R. E. On the wall structure of the turbulent boundary layer, *J. Fluid Mech.*, 1976, **162**, 389–413.
4. NARASIMHA, R. AND KAILAS, S. V. Turbulent bursts in the atmosphere. *Atm. Env.*, 1990, **24**, 1635–1645.

Thesis Abstract (Ph. D.)

Engineering behaviour of lime stabilized fine grained soils containing sulphate and the governing physico-chemical mechanisms by H. N. Ramesh

Research supervisors: P. V. Sivapullaiah and A. Sridharan
Department: Civil Engineering

1. Introduction

The aim of the present investigation is to study the engineering behaviour of fine-grained soils containing optimum lime and varying sulphate contents. The study is of great practical relevance in the context of the use of several trace inorganic chemicals to enhance the lime reactivity of soils[1]. The presence of sulphate is also reported to have adversely affected the lime-stabilized soils used for road construction[2]. Practically, no data is available on the effect of sulphate content on basic and engineering properties of lime-stabilized soils. Hence, detailed investigations have been carried out on the engineering behaviour of lime-stabilized fine-grained soils containing sulphate.

2. Experimental

The soils used in this study are essentially naturally occurring black cotton soil and red earth containing montmorillonite and kaolinite as principal clay minerals, respectively. Lime was added to these soils at 6% of volume which is optimal. However, for free swell index tests, lime content was varied between 3 and 12%. Sulphate content was varied from 0.5 to 3% by the addition of sodium sulphate or calcium sulphate. Various tests like index properties, volume change and consolidated undrained triaxial test were conducted.

3. Results and discussion

It has been shown that unusual increase in liquid limit and plasticity index of lime-treated soils occurs in the presence of sulphate. While sulphate content decreases the shrinkage limit of black cotton soil, its effect on lime-treated red earth is marginal. The changes in the index properties of lime-treated soils have been explained with respect to changes in diffuse double-layer thickness

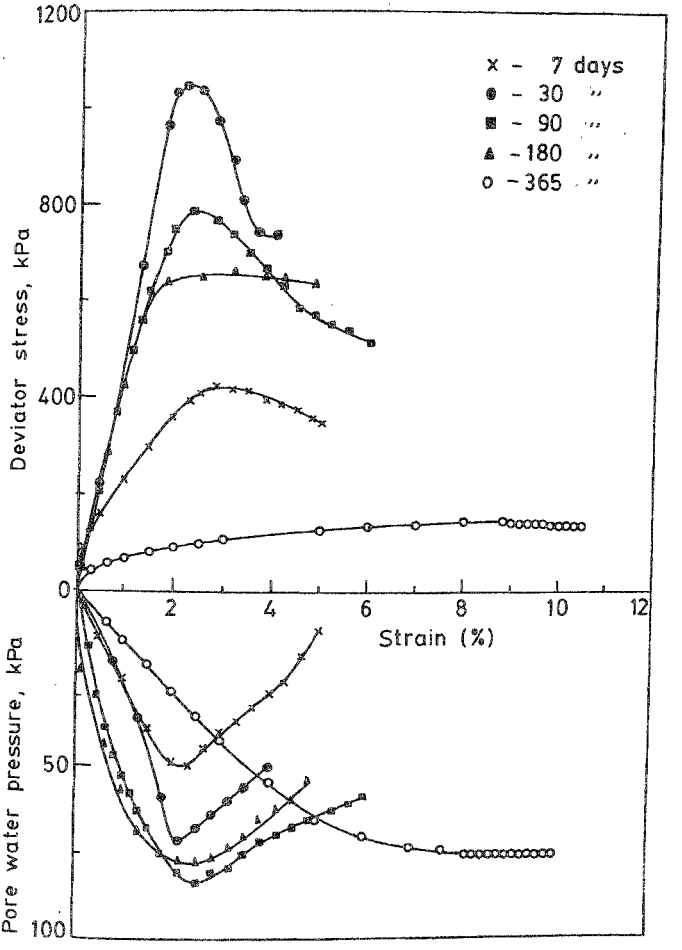

FIG. 1. Stress–strain and pore water pressure–strain behaviour of lime-treated BC soil in the presence of 1.0% Na_2SO_4 at different curing periods at a cell pressure of 100 kPa.

of clay particles, ion exchange, fabric and soil–lime–sulphate reactions. Comparison of shrinkage limit of soils with their liquid limit helped to qualitatively describe the fabric.

There are three different equilibrium free swell volumes in lime-treated soils, *viz.*, initial, maximum and final. The initial free swell volumes increase with curing due to flocculation of clay particles and reach the maximum. For naturally flocculated red earth this increase is very less. The flocculated soil particles after sufficient cementation slowly get aggregated and consolidate due to its self-weight and reach final equilibrium volume. The presence of sulphate alters all the equilibrium free swell volumes. The extent and rate of change in the free swell volumes depend on soil type, nature and amount of sulphate, apart from lime content.

While the compacted lime-treated black cotton soil showed swelling in oedometer under a nominal surcharge of 6.25 kPa, lime-treated red earth showed no swelling. This is due to flocculation of randomly oriented black cotton soil particles compared to naturally flocculated red earth particles. Further, the swelling of lime-treated black cotton soil in the presence of sulphate occurs in two distinct phases. The first phase is due to flocculation because of lime and the second is due to absorption of sulphate. For lime-treated red earth the swelling in the presence of sulphate occurs in only one stage which is due to sulphate only. The initial swelling due to lime was not observed in the case of red earth.

The variation, within small durations of curing, has been brought about by varying the duration of each pressure increment from half an hour to 24 hours. It has been shown that for lime-treated black cotton soil with any sulphate content, the primary consolidation is complete and slope of the secondary compression could be determined. The volume change behaviour of black cotton soil which is essentially controlled by diffuse double layer is increasingly controlled by shearing resistance at particle level on curing with lime. The compression of lime-treated soil with any sulphate content decreases with increase in the duration of loading, *i.e.*, with increase in the duration of curing. However, sulphate has shown different effects at different durations of loading on lime-treated black cotton soil. The presence of sulphate increased compression for a very small duration of loading of half an hour, decreased for any duration of loading of 1 to 4 hours and has no effect on the duration of loading of 24 hours.

Consolidation tests carried out on lime-treated black cotton soil cured for one year with 0.5, 1 and 3% of sodium sulphate show that the presence of sulphate increases the compression of such soils. But, in the case of lime-treated red earth the compression is higher only with 1 and 3% of sodium sulphate. The compression of both the soils increases with increase in the concentration of sulphate. Both short- and long-term curing effects have been explained based on changes in lime reactivity and alteration of soil–lime reactions in the presence of sulphate.

It has been shown that the strength of lime-treated soil increases with increase in curing periods in the absence of any sulphate content. Also, the strength of lime-treated black cotton soil in the presence of sulphate increases after small curing periods. This has been attributed to the enhancement of lime reaction of soils in the presence of sulphate. But, after curing for long periods, the peak stresses reduced in the presence of even small amount of sulphate. The reduction is higher with sodium sulphate than with calcium sulphate (Fig. 1), and is maximum with 1% of sodium sulphate or calcium sulphate at the end of one year. This has resulted in producing the stress–strain curves similar to uncemented soils. Reduction in c' occurred without affecting θ' values. This has been attributed to the breakage of cementation bonds due to alteration of soil–lime reactions in the presence of sulphate, leading to the formation of Ettringite which causes expansion and decementation of bonds brings reduction in the (A–R) forces. This reduction in strength also results in higher A_f values and curved effective stress paths.

The presence of sulphate is undesirable for strength improvement of red earth by lime stabilization. However, reduction occurs very slowly in the strength of lime-treated red earth in comparison to lime-treated black cotton soil.

4. Mechanism

Though the presence of sulphate cannot affect cation exchange reactions, it can change the fabric of soil by sulphate adsorption. The reaction mechanism by which lime reactivity can be enhanced at small curing periods has been explained. Also, it has been shown how long-term changes in soil–lime reaction products can occur. The formation of new types of compounds has been supported by X-ray diffraction study and by scanning electron microscope photographs.

5. Remedial measures

Based on the understanding of the mechanism involved in soil–lime–sulphate reaction, a method to arrest or reduce the harmful effect of sulphate has been developed. It involves the use of barium chloride in 2:1 proportion of the weight of sulphate. It has been shown that barium chloride, though less beneficial than sulphate at small curing period, will inhibit the harmful long-term effect of sulphate.

References

1. DAVIDSON, D. T , MATEOS, M. AND BARNES, H. F. — Improvement of lime stabilization of montmorillonitic clay soils with chemical additives, *Highway Res. Rec. Bull.*, 1960, **262**, 33–50.

2 DAL HUNTER — Lime induced heave in sulphate bearing clay soils, *J Geotech. Engng Div. ASCE*, 1988, **114**, 150–167

Thesis Abstract (M. Sc. (Engng))

Model reference adaptive control of unknown nonminimum phase plants by H. N. Shankar

Research supervisor: M. A. L. Thathachar

Department: Electrical Engineering

1. Introduction

In many adaptive control situations it is desirable to eliminate or minimize the disparity between the output of the plant and the desired output. In the *indirect* model reference adaptive control (MRAC) approach, the unknown parameters of an explicitly chosen model of the plant are estimated[1]. When even an upper bound on the order of the plant is unknown, order estimation techniques are resorted to[2]. Alternatively, in *direct* MRAC the controller is directly adjusted to minimize the error between the plant and the model outputs[3]. An independent direction, recently explored, is the *command generator tracker* (CGT) method[4].

Direct MRAC and the CGT approaches call for certain precise *a priori* structural information of the plant, one such being the order information[5,6]. Frequently, systems in practice have orders much in excess of those assumed. It is well known that several algorithms become unstable or even explode in the presence of even 'small' unmodelled dynamics or noise[7,8]. Also, strict positive realness (SPR) or almost SPR (ASPR) plays a pivotal role in the design of adaptive controllers.

The plant being in minimum phase is another, rather restrictive, yet vital, demand made in adaptive control literature. Further, with a nonminimum phase plant, matching of the closed-loop and the reference model transfer functions cannot, in general, be assured; for the inverse of a nonminimum phase plant, if it exists, is unstable and the error cannot be asymptotically forced to zero for all inputs. Consequently, adaptive tuning of systems which are allowed to be in nonminimum phase must be over some constrained class of inputs.

2. The problem

The problem solved in the present research work is as follows: Given a finite-dimensional, dynamical, LTI, single input single output (SISO), unspecified plant which may be either in minimum or nonminimum phase, which need not be ASPR, the order (or even an upper bound on the order) of which is unknown, and given a fully specified desired reference model, generates the plant command such that the output of the plant matches or approximates the output of the model.

The reference model, specified by means of a transfer function, and the unknown plant have to be asymptotically stable, strictly proper and lacking zeros on the $s = j\omega$ axis; they are, however, allowed to have zeros on both sides of the $s = j\omega$ axis. The zeros of the model and the plant need not have matching locations.

The model input is not specified *a priori* save that it belongs to a prescribed class. It may be:

(i) Step-like; *i.e.*, asymptotically approaching a final value

(ii) Sinusoid-like; *i.e.*, asymptotically approaching a sinusoid of any frequency

(iii) A combination of 1 and 2 above

(iv) A combination of 1 and finitely many sinusoids.

3. Contribution of the thesis

Some preliminary results to be used in the thesis are stated in the form of propositions and proved. Inputs that smoothly approach constant nonzero values are considered first. A performance index that is to be minimized is chosen and its significance brought out. An ε-optimal law (specified by Algorithm $\mathcal{A}_f$) is developed in stages, throwing light on the process in its different functional aspects, *viz.*, amplitude matching and sign matching.

A class of inputs that asymptotically approach a sinusoid of nonzero amplitude and any frequency is defined. As before, relevant performance index is defined. Through a series of lemmas, a condition sufficient for optimizing the performance is obtained. There is, in general, a requirement for an appropriate phase shift to be introduced. As the incorporation of this required phase shift needs information of the frequency, a scheme to identify the frequency of the signal which the plant output approaches is devised. An algorithm $\mathcal{A}_s$ is proposed and is shown to ensure ε-optimality, *i.e.*, asymptotic matching of the amplitude, frequency and phase between the model and the plant outputs is established.

For model inputs belonging to class 3 (those that tend to a sinusoid with an offset) a comprehensive performance index which essentially subsumes the performance indices of the earlier chapters is selected. The control law obtained through Algorithm $\mathcal{A}_c$ has two components — dc and ac. For inputs of the form '$A + B \sin \omega t$', the dc and ac components are extracted and separated. Here also, the frequency of the ac component is identified and the required phase shift determined. The two components are then multiplied by appropriate gains which are computed

adaptively and online. The amplified/attenuated components are then added to give the control law. Boundedness of the controller gains, stability of adaptation and ε-optimality of the law have been established. That is, the error between the dc components, the disparity between the amplitude, frequency and phase of the ac components of the plant and the model outputs go arbitrarily close to zero asymptotically. The algorithm $\mathcal{A}_c$ is a generalization over the earlier two algorithms $\mathcal{A}_f$ and $\mathcal{A}_s$ proposed for inputs of classes 1 and 2.

With inputs comprising an offset and sinusoids of multiple frequencies application of Algorithm $\mathcal{A}_c$ shows that the offsets and the r.m.s. of the oscillating components of the plant and the model outputs match asymptotically. Stability in the presence of noise is discussed.

All the algorithms proposed in this thesis are shown to be robust with respect to initial conditions.

Finally, simulations that illustrate the efficacy of the different control laws contained in the three chapters in adaptively tuning both minimum and nonminimum phase plants are presented.

4. Conclusions

Adaptive control of asymptotically stable plants whose order or even an estimate of the order is unknown and which are allowed to have nonminimum phase zeros is attempted employing a completely time-domain approach. Performance indices that capture all of the following aspects of the problem are chosen: (a) the nature of the unknown plant, (b) the characteristics of the fully specified desired reference model, (c) the properties of the class of inputs, and (d) the goal. They incorporate the disparity between the plant and the model outputs. Sufficient conditions for driving the index to an arbitrarily small neighbourhood of zero are obtained through a sequence of suboptimal laws. These form the bedrock for the development of schemes with feedback compensation. The control law proposed is *not* of the PID form. It is nonlinear in the inputs and outputs of the plant and the model. The output and error do, however, influence the control law; hence the reference to feedback.

The thesis builds up the complexity of the suggested schemes in a gradual manner. As the class of inputs grows in complexity, so does the corresponding algorithm. It is rigorously established that in every case, the scheme ensures convergence of the plant output to an arbitrarily small neighbourhood of the output of the model. The controller remains bounded in the process.

Extension from SISO to MIMO plants, wider class of model inputs, possible relaxation of the condition that the plant be asymptotically stable are but a few of the possible avenues for further investigations.

The work reported in this thesis does not, *per se*, fall into any of the specific types catalogued in the literature on adaptive control due to three considerations — the type of plants investigated, the class of model inputs considered and the nature of control law proposed.

References

1. LJUNG, L. *System identification: A theory for the user*, 1987, Prentice-Hall.

2. SLIWA, S. M. *An on-line equivalent system identification scheme for adaptive control*, Ph. D. thesis, Department of Aeronautics and Astronautics, Stanford University, Stanford, 1984.

3. ASTROM, K. J. Adaptive feedback control, *Proc. IEEE*, 1987, **75**, 185–217.

4. BARKANA, I., KAUFFMAN, H. AND BALAS, M. J. Model reference adaptive control of large structural systems, *AIAA J. Guidance Control*, 1983, **6**, 112–118.

5. NARENDRA, K. S. AND ANNASWAMY, A. M. *Stable adaptive systems*, 1989, Prentice-Hall.

6. SASTRY, S. AND BODSON, M. *Adaptive control—Stability, convergence and robustness*, 1993, Prentice-Hall of India, New Delhi.

7. ROHRS, C. E., VALAVANI, L., ATHANS, M. AND STEIN, G. Robustness of adaptive control algorithms in the presence of unmodeled dynamics. *Proc. 21st IEEE Conf. on Decision and Control*, Florida, 1982, pp. 3–11.

8 ROHRS, C. E., VALAVANI, L., ATHANS, M. AND STEIN, G. Robustness of continuous-time adaptive control algorithms in the presence of unmodeled dynamics, *IEEE Trans.*, 1985, **AC-30**, 881–889.

Thesis Abstract (M. Sc. (Engng))

Finite element analysis of laminated pressure bottles by V. Rajasekhar

Research supervisor: A. V. Krishna Murty

Department: Aerospace Engineering

1. Introduction

Pressure vessels find extensive application in several engineering disciplines such as civil, mechanical, chemical and aerospace. A pressure bottle is essentially a small pressure vessel used in satellites for station-keeping purposes. Traditionally, light metals with high-specific modulus and strength are used for such applications. With the availability of composite materials and the possibility of designing and tailoring these materials for specific applications, composite materials in the form of fibre-reinforced plastics have become attractive candidates for application to pressure bottles in satellites. Unfortunately, the analysis and design of composites is much more complicated than metallic structures and requires efficient computational tools to evaluate necessary stresses. In addition, the possibility of unavoidable defects during manufacture and damages during service becomes an important concern in the design of such pressure bottles. The ability to accurately estimate the interlaminar stresses is an essential prerequisite for devising methodologies to identify probable damage sites or critical zones and for formulating damage-tolerant analysis strategies. In the current literature the development of the methods of estimating interlaminar stresses in laminated structures is receiving a great deal of attention. The main objective in this thesis is to develop methods for estimating interlaminar stresses in laminated pressure vessels.

2. Contribution of the thesis

It is generally found that classical laminated shell theory is adequate to estimate inplane stresses with reasonable accuracy. Recent studies[1,2] have also indicated a possibility of obtaining interlaminar stresses in thin shells using classical thin shell theory, by adopting the method of integrating local equilibrium equations. Following this approach, a laminated conical thin shell element has been developed for the analysis of laminated shells. The interlaminar stresses are obtained by integrating the shell equilibrium equations. Solutions based on classical laminated shell theory are not always adequate, particularly in regions where interlaminar stresses are large, such as geometric discontinuities and hence three-dimensional finite-element analysis may be consid-

ered unavoidable. Finite-element solutions based on three-dimensional elements are not only expensive, but also need large computational facilities. A simpler approach known as global–local approach has been adopted to generate solutions in local regions, where the classical shell theory is considered inadequate.

Based on the comparative study of the results of cylindrical shells it is observed that the laminated conical shell element can give reasonably good estimates of interlaminar stresses in cylindrical shells. A laminated pressure bottle of variable thickness with an aluminium liner has also been analysed using the conical shell element. However, unlike the case of simple cylindrical shells, the presence of ply drops, reinforcements in the form of hoop winding and thickness variations require the use of three-dimensional elasticity solution, at least locally near such discontinuities. To bring out this aspect, a three-dimensional elasticity solution has been generated using an axisymmetric element for layered cylindrical shells which also served as a benchmark solution, against which simpler finite-element solutions are assessed[3]. However, in the analysis of pressure bottles a fine finite-element mesh is needed in certain regions where the thickness has a discontinuity and also near the junctions of end closures with cylindrical shell. Since the complete three-dimensional solution is expensive, a global–local finite-element strategy is employed using the three-dimensional axisymmetric element, to analyse the pressure bottle. Through this study, it has been demonstrated that the global–local approach offers a convenient way of obtaining detailed local solutions. This method is general and can be implemented with any general-purpose software.

Reference

1 ENGBLAM, J J. AND ÖZEN, O. O. — Finite element formulation including interlaminar stress calculation, *Comput. Struct.*, 1986, **23**, 241–249.

2. KRISHNAMURTY, A V AND HARIKUMAR, H K — Modeling of symmetric laminates under extension, *Composites Struct.*, 1989, **11**, 15–32.

3 KANT, T AND MENON, M. P — Estimation of interlaminar stresses in fibre reinforced composite cylindrical shells, *Comput. Struct.*, 1991, **38**, 131–147.

Thesis Abstract (M. Sc. (Engng))

Simulation of microstructural evolution during grain growth and recrystallization

by N. Krishnan

Research supervisors: S. Ranganathan, A. K. Lahiri and S. Seshan

Department: Metallurgy

1. Introduction

The microstructure of a material is an important factor in determining a number of its properties. The complete analytical prediction of microstructural evolution in materials has not been easy mainly due to the complexity of grain interactions. The evolution of the microstructure depends primarily on the precise specification of the coordinates of the grain boundary network, the crystallographic orientation of the individual grains and the mechanism by which the elements of the boundary are postulated to move. However, with the advent of powerful computers, it is now possible to simulate the microstructural evolution during grain growth.

Major reviews on microstructural evolution have been written by Atkinson[1] on grain growth, Glazier and Weaire[2] on the topological aspects of grain growth and by Anderson[3] on the computer simulation of grain growth. Srolowitz[4] has edited books on computer simulation of microstructural evolution. A major review on recrystallization has been written by Cahn[5].

2. Algorithm

A probabilistic method employing the Monte-Carlo technique has been used in the present investigation. The microstructure is mapped on to a discrete lattice. The orientation of the different grains is expressed in terms of an index referred to as the 'orientation number'. A grain boundary is defined to lie between sites of differing orientation. The energy of the system is described in terms of the 'lattice site energy' E_1, the energy of each site, is defined as

$$E_1 = (-J)\sum_{j \in nn}\left(\delta_{qiqj} - 1\right)$$

where J is the magnitude of the grain boundary energy, δ_{qiqj}, the Kronecker delta, qi and qj refer to the orientation of the site i and j, respectively. The summation is over all neighbouring orientations. The total energy of the system, E, is given by

$$E = 1/2\sum_{i=1}^{N} E_1$$

where E_1 is the energy of site i and N, the total number of sites. The factor 1/2 accounts for each boundary segment being counted twice.

The kinetics of the boundary motion is simulated using a Monte-Carlo technique. A site is selected at random and its orientation is changed randomly to any of the other Q-1 orientations, selected randomly. The change in the energy before and after the change, δE, is calculated. The change is accepted,

(i) with probability 1 if $\Delta E < 0$

(ii) with probability 1/2 if $\Delta E = 0$

(iii) with probability $\exp(-\Delta E/kT)$ if $\Delta E > 0$, where k is the Boltzmann constant and T, the absolute temperature.

The time scale for the simulation is based on the number of reorientation attempts made. The unit time is defined as 1 Monte-Carlo step (MCS), which is N reorientation attempts (N-total number of sites). This is subject to the condition that no reorientation attempt on all the other sites is done. Periodic boundary conditions are imposed on the structure so that it is treated as one unit cell in an infinite microstructure. A 100×100 simulation lattice was chosen. The simulations were carried in 2-D applying periodic boundary conditions.

The model incorporates both the factors involved in grain growth–surface tension equilibrium and topological requirements of space filling. In the case of recrystallization, the model also takes the magnitude of stored energy into account.

For recrystallization, the lattice site energy is modified as

$$E_1 = H * \theta(Q - S_1) + (-J)\sum_{j \in nn}\left(\delta_{qiqj} - 1\right).$$

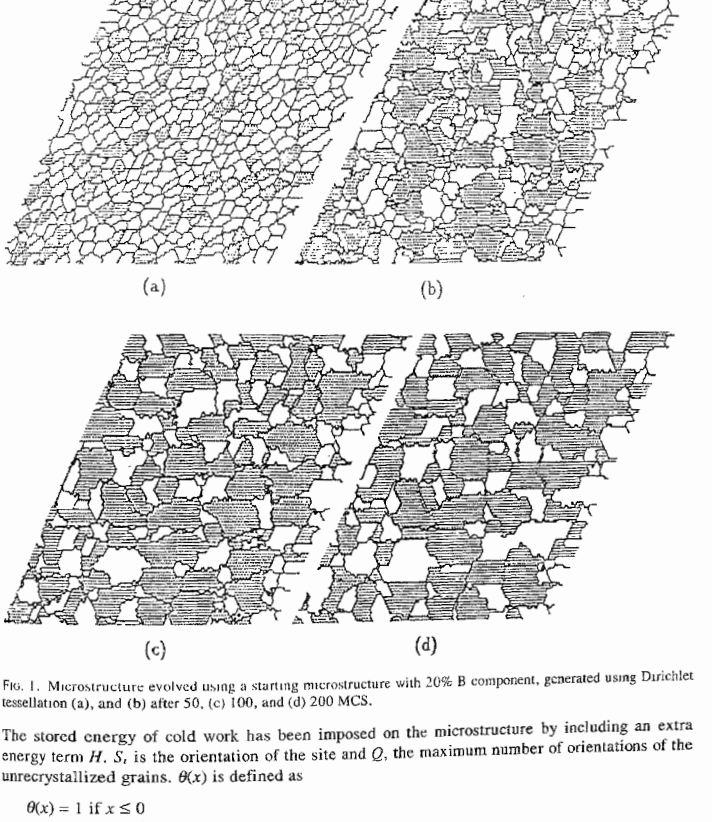

FIG. 1. Microstructure evolved using a starting microstructure with 20% B component, generated using Dirichlet tessellation (a), and (b) after 50, (c) 100, and (d) 200 MCS.

The stored energy of cold work has been imposed on the microstructure by including an extra energy term H. S_i is the orientation of the site and Q, the maximum number of orientations of the unrecrystallized grains. $\theta(x)$ is defined as

$$\theta(x) = 1 \text{ if } x \leq 0$$
$$= 0 \text{ if } x > 0.$$

3. Results and discussion

For investigations of grain growth, the simulations were carried out with and without considering initial textures and in the presence of texture. In the absence of texture, grain growth was simu-

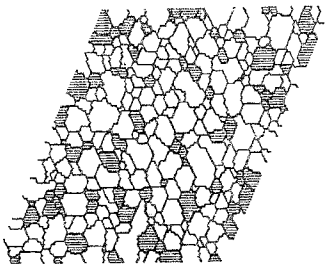

FIG. 2. Starting microstructure with 20% of B component grains generated using the Monte0Carlo simulation.

lated to determine the effect of the number of orientations (Q) and the temperature factor. From the simulation results, it was found that in random coalescence of the grains, $Q \geq 32$ was required (Fig. 1). A growth exponent of 2.39 ± 0.17 was obtained for $Q \geq 32$. From the topological information, special statistical linear relationships between the number of edges and the normalized grain radii were obtained.

The effect of texture on grain growth was simulated considering two texture components A and B. The texture effect was incorporated by assuming low-angle boundaries to exist between grains of the same texture component and high-angle boundaries existing between grains belonging to different components. The experimentally observed spread of orientation was included in the simulation. The simulation was carried out for different fractions of the two components. The ratio of the energy of the low-angle boundary to that of the high-angle boundary (Γ_{AA}/Γ_{BB}) was varied from 0.1 to 0.9. It was found that the grain growth is dependent on the initial microstructure. For a starting microstructure generated using Dirichlet tessellations (Fig. 2) it was found that the grain growth kinetics follows a parabolic growth law ($n = 2.1 \pm 0.1$). The grain size distribution was found to be log–normal as was the size distribution of the individual component grains. When the starting structure used (Fig. 3) was generated using a grain growth from a size of 1 site/Monte-Carlo step (MCS), it was found that the microstructure does not reach a scaling state. The grain growth kinetics was not parabolic and n was found to be 2.95 ± 0.15. The change in the fraction of the two components was found to be dependent on the value of (Γ_{AA}/Γ_{BB}). It is found that the fraction of the minor component increases with time and ultimately becomes the major component. But no oscillation between the two textures is seen. The increase in the frac-

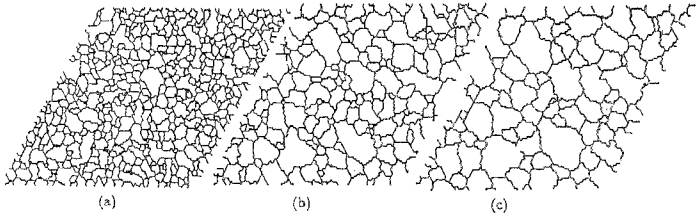

FIG. 3. Microstructure evolved with $Q = 32$. (a) 100, (b) 500, and (c) 1000 MCS.

tion of the minor component varies with the value of $(\Gamma_{AA}/\Gamma_{BB})$ and is found to be higher for value of $(\Gamma_{AA}/\Gamma_{BB})$. No increase is found for a value of 0.9 and the fraction of the minor component decreases and eventually goes to 0 for values of $(\Gamma_{AA}/\Gamma_{BB}) > 1$. The change in the fraction of the minor component is attributed to these grains being surrounded by high-angle boundaries. It is obvious that the probability of these grains being surrounded more by grains of the major component than by grains of the same component is higher.

The simulation of recrystallization was carried out for uniform as well as nonuniform conditions of the stored energy in the microstructure. Both equiaxed grain structure and elongated grain structures have been considered. The critical size of the nuclei which will grow but not shrink without regard to its location in the microstructure has been estimated by placing a single nucleus in a deformed matrix. The simulation was varied for the conditions of the nucleation taking place at a constant rate as well as under site-saturated condition. Nucleation rates varying from 1 to 10 site/MCS were considered for continuous nucleation, and 25 and 350 nuclei for site-saturated nucleation. The stored energy of cold work was varied by changing the ratio of the stored energy term, H, and the magnitude of the grain boundary energy, J, between 6 and 0.25. It was observed that the Johnson–Mehl–Avrami–Kolmogorov (JMAK) exponent varies with the number of nuclei as well as the H/J ratio. The global migration rate was estimated using the Cahn–Hagel formula and was found to be independent of the number of nuclei, but lower for lower H/J values. The grain size distributions for site-saturated and continuous nucleation were found to be different. The results were explained in terms of the growth rate and impingement effect.

References

1. ATKINSON, H. V. — Theories of normal grain growth in pure single phase systems, *Acta Metall.*, 1988, **36**, 469.
2. GLAZIER, A. J. AND WEAIRE, D. — The kinetics of cellular patterns, *J. Phys.: Condensed Matter*, 1992, **4**, 1867.
3. ANDERSON, M. P. — Annealing processes—Recovery, recrystallization and grain growth (N. Hansen *et al.*, eds), *7th Riso Symp. Metallurgy and Materials Science*, 1986, p. 15.
4. SROLOWITZ, D. J., GREST, G. S. AND ANDERSON, M. P. — Computer simulation of grain growth: V. Abnormal grain growth, *Acta Metall.*, 1985, **33**, 2233.
5. CAHN, R. W. — In *Physical metallurgy*-II (R. W. Cahn and P. Haasen, eds), p. 1595, 1983, North-Holland Physics Publishing.

Thesis Abstract (M. Sc. (Engng))

Development of an automated high pressure–high temperature system for electrical studies by T. K. Mondal

Research supervisor: S. Asokan

Department: Instrumentation and Services Unit

1. Introduction

Combination of high pressures and high temperatures is useful in a variety of areas[1]. In the present work, an automated high pressure–high temperature system for electrical resistivity measurements up to 8 Gpa pressure and 400°C temperature has been developed (Fig. 1).

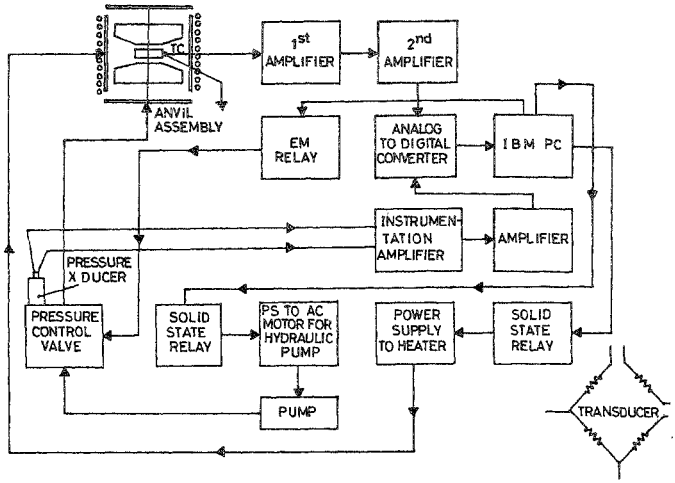

FIG. 1. Block diagram of the high pressure–high temperature system.

2. The design aspects of the high pressure–high temperature system

The high pressure–high temperature system consists of an opposed anvil high-pressure device made of tungsten carbide (12 mm dia). The anvils are held in position using a copper guide ring and are heated externally by a cylindrical heater placed around the copper ring. Radial and axial heat losses are reduced by providing suitable thermal insulation. Sample is contained between the anvils, in a pyrophyllite gasket assembly and its temperature is sensed by a K-type thermocouple. The thermocouple output is amplified, digitized and fed to an IBM PC through a digital input output and timer card. Decoding of the signals to corresponding temperatures and comparison of the sample temperature with the set value are done in the PC[2]. A PC-based temperature controller is employed to control the temperature to better than ±1%[3].

The Bridgman anvils are pressurized in an electrically operated hydraulic press. The applied oil pressures are read using a 400 bar thin film strain gauge pressure transducer. The transducer output is amplified, digitized and read by the PC. The hydraulic press is provided with a valve assembly to control the pressures (Fig. 2). The valve assembly consists of two directional control solenoid valves A and B, two flow regulators (for onward and return, respectively), a pressure relief valve and a pilot operated check valve. By suitably energizing the solenoids A or B, pressurization or release of the system can be achieved. The pressure relief valve ensures that the system pressure does not accidentally exceed the maximum set pressure. Snubbers are provided in the onward and return oil lines, to slow down pressurization and release.

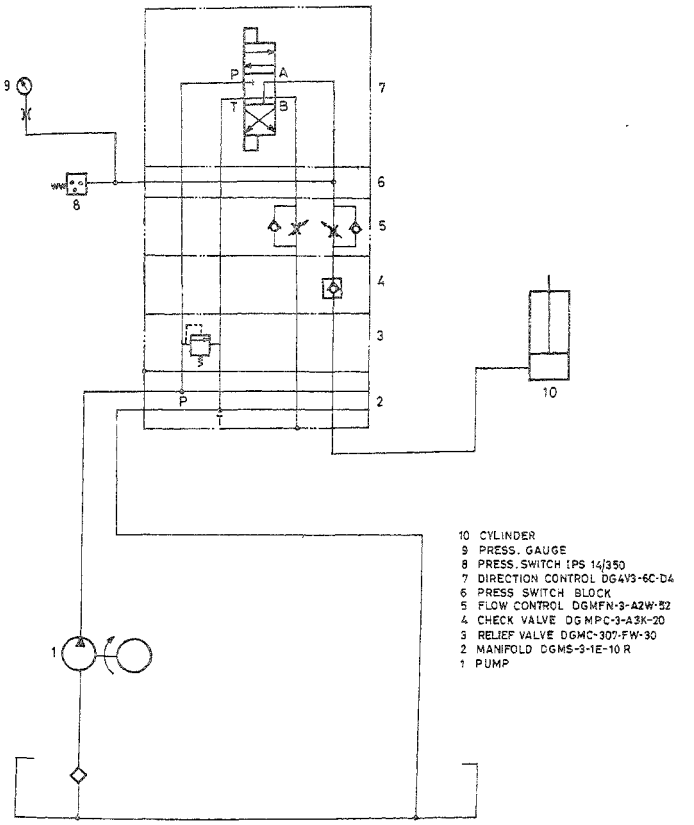

FIG. 2. Pressure control value assembly.

Depending on the difference between the system and the set point pressure, the PC sends signals to energize the proper solenoid valve. The PC also controls, simultaneously, the pumping of oil in the hydraulic press. Thus, a pressure control of ±5 psi is achieved in this set-up. The sample resistance is measured by the four-probe method. The voltage developed across the sample, on passing a constant current, is measured by a digital voltmeter interfaced current, interfaced with

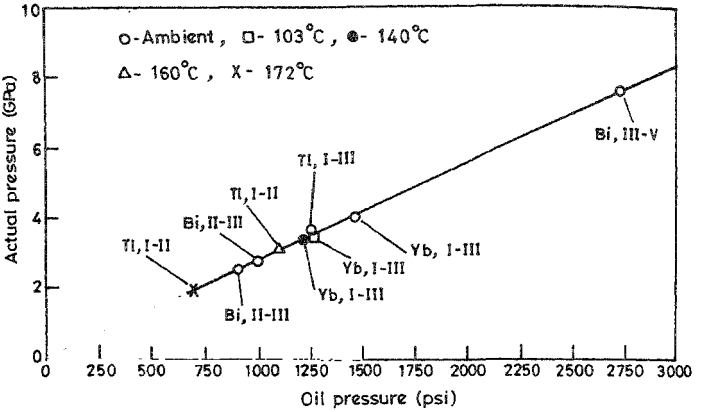

FIG. 3. The pressure calibration plot for 12-mm anvils at different temperatures.

the PC by IEEE 488. The resistivity experiment can be carried out, either by keeping the pressure constant and varying the temperature or *vice versa*. Once parameters like set pressure, tempera-

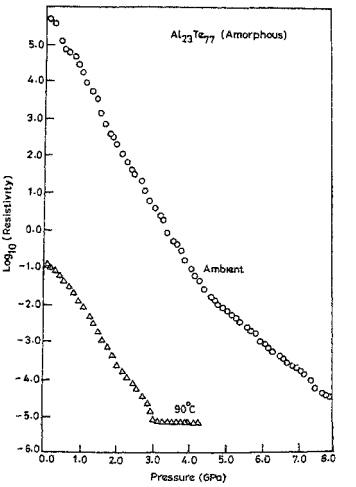

FIG. 4. The variation of electrical resistivity with pressure of $Al_{23}Te_{77}$ glass at ambient and 90°C.

ture, etc., are specified, the experiment is undertaken automatically and resistivity data at high pressures and at high temperatures are collected. Graphs of the kind, pressure *vs* time, temperature *vs* time, resistivity *vs* pressure at different temperatures are plotted and data files created.

The high- pressure–high- temperature system has been calibrated, using resistivity transitions of Bi, Yb and Tl[4]. Figure 3 shows the calibration curve obtained by plotting the oil pressures of the observed transitions against actual pressures.

3. Electrical resistivity behaviour of Al-Te glasses at high pressure and high temperature

To find the usefulness of the system developed, studies on the electrical resistivity behaviour of Al-Te glasses at different pressures and temperatures have been undertaken. Figure 4 shows the variation of electrical resistivity with pressure at different temperatures, of a representative $Al_{23}Te_{77}$ glass. It can be seen from Fig. 4 that metallization of pressures of Al–Te glasses gets reduced drastically at high temperatures.

References

1. MINOMURA, S. — *Solid state physics under pressure: Recent advances in anvil devices*, 1985, KTK.
2. KRIKELIES, N. J. — *IEEE Trans.*, 1984, **IE-31**, 65.
3. VEGTE, J. V. — *Feedback control systems*, 1986, Prentice Hall.
4. CANNON, J. F. — *J. Phys. Chem. Ref. Data*, 1974, **3**, 791.

Thesis Abstract (Ph. D.)

Immunochemical studies on the family of biotin binding proteins by N. Subramanian

Research supervisor: P. R. Adiga

Department: Biochemistry

1. Introduction

Avidin[1] from the chicken egg white, streptavidin[2] from the bacterium *Streptomyces avidinii* and biotin-binding proteins (BBP-I[3] and -II[4]) from chicken egg yolk constitute a family of proteins that bind the vitamin biotin with extremely high affinities. The yolk BBPs are involved in deposition of the vitamin in the developing oocyte in chicken whereas an antimicrobial function has been attributed to avidin. The fact that all these proteins bind the vitamin in the same manner, unlike biot-independent enzymes, indicates that the structural features involved in ligand binding could be similar, if not identical in these proteins. To delineate the basis of putative structural similarity among these proteins, studies were carried out using antibodies as immunological probes.

2. Experimental procedures

Avidin has been purified to homogeneity using a novel procedure involving ammonium sulphate fractionation, ethanol precipitation and S-Sepharose column chromatography. BBP-I and -II have been purified by employing a common method using butanol extraction, DEAE-Sephacel column chromatography, biotin-AH-Sepharose affinity chromatography and fast-protein liquid chromatog-

raphy (FPLC) system. Specific poly- and monoclonal antibodies (MAb, using the hybridoma technique[5]) have been produced to avidin and BBP-II. Influence of these antibodies on protein–ligand interaction was studied using [^{3}H]-biotin as the radioligand; fluorescence spectral characteristics were monitored using FITC-conjugated proteins. Avidin was chemically cleaved with CNBr and hydroxylamine and the peptidyl fragments were identified by N-terminal sequence analysis. Various overlapping octapeptides from avidin and streptavidin sequences were synthesized on polypropylene pins by Geysen's solid-phase peptide synthesis[6] and checked for MAb binding by ELISA technique. An 11 amino acid peptide (Y-IDRNGKEVLK) was synthesized by Merrifield's solid-phase synthesis using Fmoc chemistry. Anti-peptide antibodies were raised against the peptide conjugated to a carrier protein, diphtheria toxoid, and used to study their influence on protein–ligand interaction.

3. Results and discussion

Two representative monoclonals B12C8 and H12G4 for avidin and one for BBP-II, *viz.*, B5B5 were selected. Their subclass isotyping revealed that they all belonged to IgG1, K type. Avidin polyclonal and monoclonal antibodies showed very good reactivity with streptavidin but to a relatively lesser extent with BBP-I and -II in Western blot analysis and liquid-phase radioimmunoassays. On the other hand, the poly- as well as monoclonal antibodies to BBP-II significantly cross-reacted with both streptavidin and avidin in addition to BBP-I. These studies reveal the distinct possibility of the existence of common epitopic structures on the surface of these molecules. Interestingly, both poly- and monoclonal antibodies to avidin, as well as to BBP-II, could release the bound biotin from the interior of these molecules and could additionally inhibit the binding of biotin to the apo-protein forms of avidin. BBP-II and streptavidin. Since antibodies recognize only the surface periphery of an antigen, it was speculated that the influence of these antibodies, in terms of displacing the bound biotin, is attributable to interference with necessary conformational changes consequent upon ligand binding. To monitor such changes, fluorescence spectral characteristics were monitored using FITC-conjugated proteins. It could be shown that upon biotin binding to FITC-avidin, there occurs a two-fold enhancement in the fluorescence intensity while corresponding increase with FITC-streptavidin was seven fold. Both poly- and monoclonal antibodies to avidin (and BBP-II) effectively quenched the enhanced fluorescence observed when biotin bound to either FITC-avidin or FITC-streptavidin. This conclusively proves that upon antibody interaction with specific antigenic determinant(s) on these biotin-binders, ligand binding is curtailed due to 'freezing' of induced conformational changes essential to maintain liganded state. In view of the fact that avidin–biotin interaction is the strongest protein–ligand interaction known in nature, it is of interest to identify this critical structural feature shared by all the three proteins, and the location of the same in the 3-D structure of the proteins where known.

Because of its relative abundance and ready availability, avidin was chosen as a representative molecule for further studies on these lines. Avidin is a homotetrameric protein with each subunit containing 128 amino acids; to simplify the procedure it was decided to obtain minimized fragments of avidin with relevant immunoreactivity associated with it. Several well-established proteolytic enzymes were tried for specific cleavage but none of them was capable of cleaving avidin into reliably discrete fragments with associated antigenic reactivity. Hence, chemical cleavage approach using CNBr and hydroxylamine was resorted to exploiting the fact that there are two methionine residues (positions 18 and 96) and one Asn-Gly peptide bond (position 88-89), the known cleavage sites for CNBr and hydorxylamine, respectively. The resulting fragments were resolved by tricine SDS-PAGE and after N-terminal sequence analysis, the five CNBr frag-

ments were identified to be: 17 K (1–128, intact subunit), 15 K (1–96), 12 K (19–128), 8 K (19–96), 4 K (97–128) and the three hydroxylamine fragments to be: 17 K (1–128), 10 K (43–104), 8 K (58–104). When blots containing these fragments were probed with either poly- or monoclonal antibodies (to avidin as well as to BBP-II) it could be shown that except the CNBr 4 K fragment, all the other fragments obtained were recognized by antibodies. The minimal fragments in size which still showed reactivity with the antibodies were the 8 K fragments (19–96/CNBr, 58–104/hydroxylamine). Polyclonal antibodies to these truncated avidin fragments also could release bound biotin as well as inhibit binding of biotin to all the three apoproteins. This finding suggested that the stretch of residues common to both the 8 K fragments (58–96) harbours the antigenic determinant(s) in question. To precisely identify and locate the epitope in the sequence, overlapping octapeptides were synthesized on polypropylene pins by Geysen's solid-phase peptide synthesis and corresponded to both the avidin and streptavidin sequences matching in this region. These multiple pin-bound peptides were probed with both mono- and polyclonal antibodies. From the pattern of reactivity in ELISA it could be shown that there is a critical region comprising a minimal sequence of ^{87}RNGK^{90} in avidin and ^{84}RNAH^{87} in streptavidin reactive with the monoclonal antibodies. Both these structural features are parts of β-turn conformations, *i.e.*, they are located in loops that are surface exposed, as evident from the ribbon models of the proteins obtained from X-ray crystallographic analysis[7,8]. Two additional epitopic sites at the flanking regions in both avidin and streptavidin are identifiable when probed with avidin polyclonal antibodies. Despite the fact that they are raised against two different proteins, avidin MAb H12G4 and BBP-II MAb B5B5 exhibited a similar pattern of reactivity with synthetic peptides corresponding to both avidin and streptavidin sequences. This shows that they recognize an epitopic conformation comprising chemically similar amino acids if not identical residues. The other avidin MAb B12C8 seems to recognise a relatively larger overlapping core sequence when compared to that by the other MAbs. Nevertheless this MAb also recognized peptides having minimal sequences of 'RNGK' as in avidin and 'RNAH' as in streptavidin.

To generate anti-peptide antibodies towards the critical epitopic structure, a 11 amino acid peptide (Y-IDRNGKEVLK) with a tyrosine residue at the N-terminus, to facilitate coupling to the carrier protein, *viz.*, diphtheria toxoid, was synthesized by Merrifield's solid-phase peptide synthesis using Fmoc chemistry. After cleavage from the resin the peptide was further purified using HPLC and the purity of the peptide was ensured by reverse-phase HPLC and amino acid composition. The purified peptide was coupled to the carrier protein using activated bis diazobenzidine. The conjugated peptide elicited a good antibody response as revealed by its high titre which reflects its highly immunogenic nature. This anti-peptide antiserum recognized native avidin, streptavidin and BBP-II in ELISA and on Western blot analysis. Moreover, this anti-peptide antibody was capable of bringing about drastic inhibition of [^{3}H]-biotin binding to all the three apoproteins as well as displacing bound biotin from the three holoproteins thus mimicking both the poly- and monoclonal antibodies in this regard. This confirms the results observed with the MAbs and underscores the importance of a single crucial epitopic conformation on these molecules in maintaining the ligand-binding characteristics. It is known that avidin-bound biotin can be released only by very harsh physical conditions such as treatment with 6 M guanidine hydrochloride at pH 1.5 or upon autoclaving at 120°C for 15 min. The fact that these antibodies are almost equipotent in terms of releasing bound biotin under mild experimental conditions underscores the importance of immunological approaches to interfere with high-affinity biological interactions.

References

1. GREEN, N. M. *Methods Enzymol.*, 1990, **184**, 51–67.

2.	CHOIET, L. AND WOLF, F. J.	*Arch. Biochem. Biophys.*, 1964, **106**, 1–5.
3.	BUSH, L. AND WHITE, H. B. III	*J. Biol. Chem.*, 1989, **264**, 5741–5745.
4.	MURTHY, C. V.,R. AND ADIGA, P. R	*Biochim. Biophys. Acta*, 1984, **786**, 222–230.
5.	KOHLER, G. AND MILSTEIN, C.	*Nature*, 1975, **256**, 495–497.
6.	GEYSEN, H. N., MELOEN, R. H. AND BARTELING, S. J.	*Proc. Natn. Acad. Sci. USA*, 1984, **81**, 3998–4002.
7.	LIVNAH, O., BAYER, E. A., WILCHEK, M. AND SUSSMAN, J. L.	*Proc. Natn. Acad. Sci. USA*, 1993, **90**, 5076–5080.
8.	WEBER, P. C., OHLENDORF, D. H., WENDOLOSKI, J. J. AND SALEMME, F. R.	*Science*, 1989, **243**, 85–88

Thesis Abstract (Ph. D.)

A study on the photo-cross-linkable liquid crystalline polymers containing bis(benzylidene)cycloalkanones by Gangadhara

Research supervisor: K. Kishore

Department: Inorganic and Physical Chemistry

1. Introduction

Photo-crosslinkable liquid crystalline polymers have attracted considerable interest in recent years as potential candidates for applications in fields like anisotropic networks[1], nonlinear optics[2], information storage devices[3], etc. The studies so far in this class of liquid crystalline polymers (LCPs) deal with polymers containing cinnamate ester groups. These groups undergo dimerization by $2\pi + 2\pi$ cycloaddition reaction during photolysis leading to crosslinking of the chains In the present investigation, attempts have been made to synthesize and study a new class of photo-crosslinkable thermotropic liquid crystalline polymers. Synthesis of main and side-chain LCPs and side-chain liquid crystalline copolymers containing cholesteryl side group has been attempted.

To imbibe photo-crosslinking ability, the LCPs should have photoactive groups in its structure that undergo photo reaction leading to crosslinking bis(benzylidene)cycloalkanone group (Fig. 1) has been chosen as the main constituent of the polymers synthesized[4].

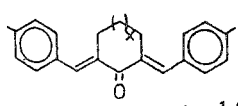

FIG. 1 $x = 1,2,3...$

This group, because of its rod-like shape, can impart liquid crystallinity to the polymer while the presence of a,β unsaturated keto functionality can make it photoactive.

2. Synthesis

(i) *Main chain liquid crystalline polymers*: Thermotropic polyesters were synthesized as shown in scheme 1.

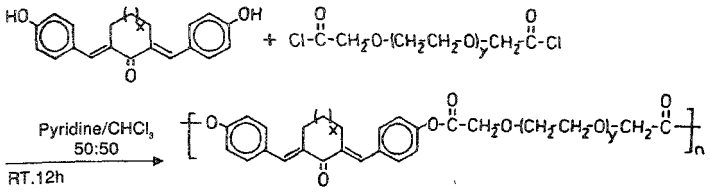

SCHEME. 1.

Both solution polycondensation and interfacial polymerization techniques were employed.

(ii) *Side-chain liquid crystalline polymers*: Side-chain liquid crystalline polymethacrylates based on cyclohexanone mesogen with four different pacer lengths were prepared by free radical initiator (Fig. 2).

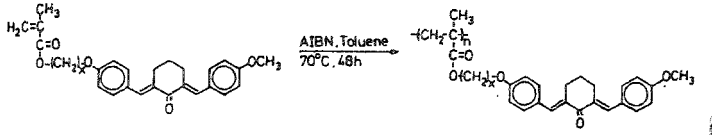

FIG. 2.

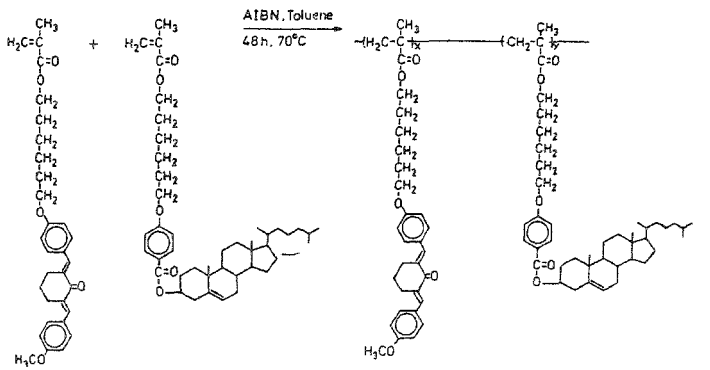

FIG. 3.

(iii) *Side-chain liquid crystalline copolymers*: These methacrylate monomers have also been copolymerized radically with cholesteric derivative of methacrylate as different compositions (Fig. 3).

3. Mesogenic properties

The mesogenic properties of these polymers were studied by polarized light optical microscope (POM) and differential scanning calorimeter (DSC). POM observation reveals that the main-chain LCPs exhibit Schlieren and threaded texture which confirms the nematic mesophase[4]. Similarly, the side-chain liquid crystalline homopolymers also exhibit nematic phase. DSC studies carried out to confirm the transition temperatures show that among the main-chain LCPs, cyclopentanone-derived polymers have higher transition temperatures while the cycloheptanone-derived polymers have the lowest. Some of the main-chain LCPs show multiple melting endotherms. Side-chain LCPs do not show melting endotherms; instead, mesophase is exhibited between glass transition temperature (T_g) and clearing temperature (T_i). The T_g decreases with increase in spacer length but no such generalization could be drawn for the T_i. For the copolymers, an increase was observed in the transition temperature with cholesteric content. The helicoidal supramolecular structure, which is a characteristic of cholesteric phase, was confirmed by circular dichroism studies.

4. Photochemistry

Photochemistry of the polymers was studied as film and in solution by UV-visible spectrophotometer. The photolysis of the polymer film in the mesophase leads to an increase in the intensity of UV-visible spectra at the initial stage and then decreases at a later stage. This increase at the initial stage of the photolysis is due to the E–Z photoisomerization of bisbenzylidene groups present in the polymer[4]. This kind of isomerization can disrupt the stacking of the chromophore pairs in the aggregate. The decrease in the intensity at a later stage of photolysis is attributed to the crosslinking reaction which involves consumption of the chromophores. After photolysis, the film was found to be solvent-resistant. The involvement of >C = C< bond present in the bisbenzylidene group in photo-crosslinking reaction has been confirmed by decrease in the intensity of >C = C< stretching band in IR spectra during photolysis, and also from model compound studies. The increase in the cycloalkanone ring size decreases the photo-crosslinking ability of the polymers.

References

1. CREED, D. *et al.* — *Mol. Cryst. Liq. Cryst.*, 1988, **155**, 57–71.
2. ULRICH, D. R. — *Mol. Cryst Liq. Cryst.*, 1990, **189**, 3–38.
3. GRIFFIN, A. C. *et al.* — *Makromol Chem. Rapid Commun.*, 1988, **9**, 463–467.
4. GANGADHARA AND KISHORE, K. — *Macromolecules*, 1993, **26**, 2995–3003.

Thesis Abstract (Ph. D.)

Kinetics of electrochemical aggregation and multiphase growth in two and three dimensions: model studies by Biplab Bhattacharjee

Research supervisor: S. K. Rangarajan

Department: Inorganic and Physical Chemistry

1. Introduction

Interfacial aggregation and growth when accompanied by electron transfer or driven by electrical field across the interface is also termed as 'electrocrystallization'. A few facets of this phenomena can be cited as: (a) varied dimensionalities observed—all the way from one dimension to fractal (*cf.* diffusion limited aggregation); (b) a plurality of mechanisms governing these—reversible adsorption–desorption (*cf.* organic films), irreversible random sequential deposition (RSA) (*cf.* deposition of composites), nucleation and growth (N/G) both in two and three dimensions (*cf.* electrodeposition), etc., and (c) a wide range of manipulations possible in the response because of the access to many variables like chemical potential and electrical potential differences, etc.

2. Multicomponent aggregation and growth models

The phenomena of interfacial aggregation and growth[1] have been studied extensively both experimentally and theoretically. Earlier modelling in this area has been restricted to simple (Avrami-like) single-component models for nucleation growth or (Ising-like) descriptions for aggregation through adsorption. Nontrivial extension of such approaches for three-dimensional growth, especially when nucleation is restricted to the substrate plane alone, was available. In the present thesis we address the following question: how does one generalise these models to reflect the presence of multicomponent simultaneously and competitively growing phases. Various multicomponent growth models developed in the present study are briefly described below.

2.1 *Adsorption–nucleation/growth*[2]

Electrochemical phase formation in two dimensions has been discussed extensively in two limits through random adsorption/desorption models and nucleation/growth models. However, current transients observed in certain experiments of underpotential deposition (upd) (*e.g.*, upd of Pb on Cu and Ag substrate) cannot be explained satisfactorily by either of the two limiting models. To understand such observations, in the present thesis, the above-mentioned models have been appropriately coupled both ways in most general form and analysed.

2.2. *Generalisation of Avrami ansatz*[2]

Avrami *ansatz* has been used extensively and successfully in the context of electrochemical phase formation and in various other areas of metallurgy to understand aggregation and growth kinetics involving single component. The *ansatz* can be expressed as

$$S = 1 - \exp(-S_x) \tag{1}$$

where S, in two-dimensional (three-) growth, is the actual area (volume) fraction transformed and S_x, the 'extended' area (volume). In the present thesis, the above result is generalized for the multicomponent growth situation and for n components it can be expressed as

$$S = 1 - \exp\left(-\sum_{i=1}^{n} S_{xi}\right) \tag{2}$$

$$S = \sum_{i} S_i \tag{3}$$

where i corresponds to the ith component. The extent of area (volume) fraction grown for each component at time t, $S_i(t)$ can be expressed as,

$$S_i(t) = \int_0^t e^{-\sum_{\mu=1}^{n} S_\mu(\tau)} \left\{ dS_{i\kappa} / d\tau \right\}_\tau d\tau. \tag{4}$$

2.3. *Hemispherical growth*[3]

The phenomenological theory of multicomponent electrochemical phase formation under varied nucleation and growth conditions has been developed using hemispherical growth model. Nucleation is restricted to the substrate alone and the randomly distributed nuclei (grown instantaneously or progressively) are allowed to grow hemispherically with specific growth rates (constant and diffusive). Avrami *ansatz* has been appropriately used to take care of the overlap effect at each cross-sectional plane followed by proper integration over the thickness of the growth to evaluate the overall extent of growth for each of the components. Among ten possible growth situations, six have been analysed in greater detail. Explicit expressions and small- and large-time behaviours of the extent growth and the corresponding current have been obtained.

2.4. *Multicomponent layer-by-layer growth*[4]

A general version of the 'cascade approach' has been developed to model the multicomponent layer-by-layer growth situation. Detailed analysis has been done for two components growing with distinct phases. The two components grow competitively and two-dimensionally in the upper layer (through direct incorporation) on top of the underlying layer with their own characteristic nucleation and growth rates. In the model developed, the fractional area covered by the component α (A and B) at the nth layer at time t, $\theta_n^\alpha(t)$ can be expressed as,

$$\theta_n^\alpha(t) = \int_0^t \left[\theta_{n-1}^A(t-\tau) f_A^\alpha(\tau) + \theta_{n-1}^B(t-\tau) f_B^\alpha(\tau) \right] d\tau. \tag{5}$$

The growth kinetics of component α at each layer have been assumed to be independent of n and expressed by $f_A^\alpha(t)$ and $f_B^\alpha(t)$, where the subscripts indicate the components in the underlying layer. $f_\beta^\alpha(t)$, $(\alpha, \beta = A, B)$, has been modelled through appropriate generalized Avrami *ansatz*. Appropriate measure of the steady-state growth and current for each of the components have been obtained.

2.5. *Random irreversible deposition*[5]

A model for the random irreversible multilayer deposition involving multicomponent has been developed. The competitive nature of such deposition processes has been taken into account at the mean field level. The kinetic equations for the coverage of the components in the nth layer have been formulated as,

$$d\theta_n^{A\alpha}(t)/dt = R_n^{A\alpha}\left[\theta_{n-1}^A(t) - \left\{ \theta_n^{AA}(t) + \theta_n^{AB}(t) \right\} \right] \tag{6}$$

$$d\theta_n^{B\alpha}(t)/dt = R_n^{B\alpha}\left[\theta_{n-1}^B(t) - \left\{ \theta_n^{BB}(t) + \theta_n^{BA}(t) \right\} \right] \tag{7}$$

where $\theta_n^{\beta\alpha}$ and $R_n^{\beta\alpha}$ (with $\beta, \alpha = A, B$) are the nth layer fractional coverages and growth rate of component α growing on the component β in the underlying layer. The extent of growth and current associated with both the components at small and large time have been analysed.

2.6. *Random sequential multilayer deposition*[6]

Random sequential multilayer deposition of different-sized k-mers simultaneously on an infinite one-dimensional substrate has been formulated and analysed for the first time. Appropriate kinetic equations have been formulated wherein the higher layer deposition rates have been modelled at the mean field level. Screening effect has been ignored. A formal solution of the rate equation has been obtained. Explicit expressions for the jamming limits and the distribution of gaps of exact sizes have been evaluated.

3. *Bridge-mediated heterogeneous electron transfer*

Fundamental description of electron-transfer rate in the context of electrodeposition (usually favoured at the defect sites) is complicated for having certain 'inner-sphere' character as well. Any model for electrodeposition at defect sites (*e.g.*, kinks) would have to calculate the electronic density of states and the localized orbitals associated with such sites. Theoretically, the presence of a chemisorbate and a defect has certain similarities (an atom missing instead of an atom on top). Most of the ingredients for the quantum mechanical formulation of defect site (or array of sites)-mediated electrodeposition are present, at the theoretical level, in the formulation of chemisorbate and chemisorbed film-mediated non-adiabatic heterogeneous electron transfer. Detailed computational studies have been taken up to understand the role of chemisorbate and chemisorbed film on the heterogeneous 'outer-sphere' electron transfer based on the formalism (using nonperturbative superoperator technique) developed earlier by Mishra and Rangarajan[7,8].

4. Discussion and conclusions

In the present thesis, several models have been developed to reflect the multicomponent nature of the aggregation and growth processes especially in the context of electrocrystallization. General formulation of the adsorption–nucleation/growth model has shown similar potentiostatic current transient features as observed in certain underpotential deposition experiments. Earlier models have been shown to result as limiting cases. Avrami *ansatz* has been generalized for multicomponent growth situations. Several growth situations in the context of multicomponent hemispherical growth have been analysed with appropriate consideration to the overlap effects. Asymptotic expressions obtained for the extent of growth can be used as diagnostic criteria for the growth mechanisms under specific growth conditions. Such studies have also suggested the existence of an asymptotic upper bound for the extent of growth of the slower growing component. For layer-by-layer growth, the steady-state current (showing Tafel behaviour) and the extent of growth for each of the components have been obtained under potentiostatic condition. Steady-state current and growth expressions have also been obtained for the random irreversible deposition models. Several limiting growth situations have also been analysed. The jamming limits for each layer have been shown to be the same in the absence of screening in the case of multilayer random sequential deposition of k-mers on an infinite one-dimensional surface. Distribution of gaps of exact sizes has also been analysed. A novel algorithm proposed for the first time to obtain the solution of the kinetic equation has been demonstrated for the dimer–trimer deposition case.

Relevance of bridge-assisted heterogeneous electron transfer in the context of electrodeposition at defect sites has been discussed. Current-potential characteristics have been obtained numerically for a lone-adsorbate-mediated anodic charge transfer at the electrode/solution interface[9]. At higher overpotential, maxima appears in the anodic current-potential plots instead of the

extended activationless region predicted by direct heterogeneous outer-sphere anodic electron transfer process. Potential and coverage dependence of the chemisorbed film-mediated anodic current at the electrode/solution interface has also been analysed[10]. The study revealed the crucial role of the density of states. Dependence of the anodic current on the adsorbate density of states, the coverage factor and other microscopic system parameters have been analysed.

References

1(a). FLEISCHMANN, M. AND THIRSK, H. R. — Metal deposttion and electrocrystallization, *Adv. in Electrochem. and Electrochem. Engng* (P. Delahay, ed.), 1963, Vol. 3, pp. 1–210.

(b). KOLB, D. M. — Physical and electrochemical properties of metal monolayers on metal substrate, *Adv. in Electrochem. and Electrochem. Engng*, (H. Gerischer (ed.)), 1978, Vol. 11, pp. 125–271.

2. BHATTACHARJEE, B. AND RANGARAJAN, S. K. — Adsorption-nucleation/growth model for electrochemical phase formation and Avrami *ansatz* for a multicomponent competitive growth process, *J. Electroanal. Chem.*, 1991, **302**, 207–218 (and references therein).

3. BHATTACHARJEE, B. AND RANGARAJAN, S. K. — Electrochemical phase formation involving multicomponents: Hemispherical overlap models for varied nucleation and growth conditions, *J. Electroanal. Chem.*, 1994, **366**, 271–286 (and references therein).

4. BHATTACHARJEE, B. AND RANGARAJAN, S. K. — Multicomponent layer-by-layer electrocrystallization: Cascade model, *J Electroanal Chem.*, 1994, **365**, 19–28.

5. BHATTACHARJEE, B. AND RANGARAJAN, S. K. — Multicomponent multilayer random irreversible deposition model: A mean field study, *J. Electroanal. Chem.*, 1994, **370**, 41–51.

6. BHATTACHARJEE, B. AND RANGARAJAN, S. K. — Random sequential multilayer deposition of different sized k-mers on a one-dimensional infinite substrate, *J. Chem. Phys.*, 1993, **99**, 8897–8907.

7. MISHRA, A. K. AND RANGARAJAN, S. K. — Theory of electron transfer process *via* chemisorbed intermediates, *J Phys. Chem.*, 1987, **91**, 3417–3425.

8. MISHRA, A. K. AND RANGARAJAN, S. K. — Electron transfer through film-covered surfaces. Case of monolayer/submonolayer–A coherent potential approximation formalism, *J. Phys. Chem.*, 1987, **91**, 3425–3430.

9. MISHRA, A. K., BHATTACHARJEE, B. AND RANGARAJAN, S. K. — Theory of electron transfer process *via* chemisorbed intermediates, Part II. Current potential characteristics, *J. Electroanal. Chem.*, 1992, **331**, 801–813.

10. MISHRA, A. K., BHATTACHARJEE, B. AND RANGARAJAN, S. K. — Electron transfer through monolayers: Dependence of current on potential and coverage, *J. Electroanal. Chem.*, 1991, **318**, 387–393.

Thesis Abstract (Ph. D.)

Electrochemistry at complex interfacial geometries by Rama Kant

Research supervisor: S. K. Rangarajan

Department: Inorganic and Physical Chemistry

1. Introduction

Real interfacial systems have complex geometries with varying degrees of irregularity or disorder. A study of electrochemical response of geometrically complex interfacial systems, *i.e.*, which assumes arbitrary or rough geometries, is a problem of long-standing and great practical importance[1–6]. The analytical approach to these class of problems is considered to be difficult. This arises from the fact that most real systems (*e.g.*, solid metal electrode) have arbitrary geometries and always possess some degree of randomness. The random surface profile of an electrode surface can be well understood by a statistical characterisation[7–9], *i.e.*, the surface structure factor of its roughness which is a gross characterisation. Unlike the less-precise fractal dimension description, this statistical characterisation does sense the global morphological details but does not demand a detailed profile of the roughness (which in a majority of cases is not available). This study has made it possible to theoretically understand the two classes of questions for nonfractal roughness.

2. The direct problems: *How roughness affects the electrochemical response of an electrode!*

2.1. *Effect of surface roughness on reversible and diffusion-limited charge transfer*[9]

A theory is developed for diffusion-limited charge transfer on a nonfractally rough electrode. The Volterra functional-like approach is applied to obtain *perturbation* expressions for the concentration, current density and measured diffusion-limited current for arbitrary one- and two-dimensional surface profiles. The random surface model is employed here for a rough electrode–electrolyte interface. In this model, the gross geometrical property of an electrochemically active rough surface—the surface structure factor—is related to the average electrode current, current density, concentration and admittance. Under the small- and long-time regimes, various morphological features of the rough electrodes, *i.e.*, excess area (related to roughness slope), curvature, correlation length, etc., are related to the (average) current transients. A two-point Padé approximant is used to develop an all-time average current expression in terms of partial morphological features of rough surface. Finally, the effect of surface roughness is studied for a specific surface statistics, *viz.*, a Gaussian correlation function. It is shown how the surface roughness enhances the overall diffusion-limited charge transfer and the average concentration of oxidised species. This work explains the short- and long-term '$1/\sqrt{t}$' behaviour and the transition region between them which was first observed by Vetter in '50s[1–3].

2.2. *Effect of roughness on the quasi-reversible charge transfer*

We develop a perturbation formalism for the quasi-reversible charge transfer on an arbitrary rough electrode. Second-order perturbation expressions are obtained for the concentration, current density, admittance and measured current transients for an arbitrary surface profile electrode. Various results obtained by earlier workers in the area of complex interfacial geometry are generalised. The results reported earlier for diffusion-limited (Nernstian) charge transfer[7–9] at an arbitrary roughness about a plane, sinusoidal, curvature expansion and realistic random surface models are generalised for the case where the effect of finite rate of charge transfer are incorporated. The problems of screened electrostatic potential of electric double layer for the one-dimensional arbitrary roughness are generalised for two-dimensional arbitrary surface. In the random surface model, the gross geometrical property of an electrochemically active rough surface, the surface structure factor is related to the average electrochemical current, the current density and the concentration. Under small- and long-time regimes, various morphological features of the rough electrode, *i.e.*, roughness factor (related to excess area and slope due to rough-

ness), curvature, correlation length, etc., are related to the (average) current transients. Finally, the effect of surface roughness is studied for a specific surface statistics, *viz.*, a Gaussian correlation function. It is shown how roughness and kinetic factors affect the overall quasi-reversible charge transfer current.

2.3. *Arbitrary shape electrode: A multiple scattering formalism in surface curvature*

The *nonperturbative* analog of the above problems is obtained using the Balian–Bloch–Duplantier multiple scattering method[10,11]. Multiple scattering expressions are obtained for the concentration, current density, current and mass-transfer operator on an arbitrary interfacial geometries in terms of local surface curvatures. These results are obtained under various boundary conditions (b.c.), *viz.*, facile (Dirichlet's b.c.), sluggish (Neumann's b.c.) and finite (radiation b.c.) surface charge transfer conditions. The effectiveness of the 'mass-transfer operator' approach is demonstrated in this formalism.

3. The inverse problems[7,8]: ***Can one electrochemically measure the statistical morphology of a rough electrode?***

For answering this novel question we develop a theory for an electrochemical way of measuring the statistical properties of a rough electrode. In this work, we show that the deviation of current transients for a rough electrode from a smooth electrode under a potentiostatic condition consists of rich morphological information regarding the rough surface. It is thus possible to measure the statistical morphology of a rough electrode (of average separation between consecutive peaks and valleys between the range of submicrometer to millimeter for a low roughness factor surfaces). It is pointed out that the normalized average current transient will have three distinct regions. The first region is of short time, the second of intermediate time and the third of long time. The short- and long-time normalized current transients are linear plots whose slope and intercept contain average morphological information. This information can be used to construct a polynomial approximation of the correlation function of the rough surface. The intermediate time current transients can be exploited to obtain formulae for the surface structure factor for both corrugated and isotropic rough surfaces. The equations connecting inner and outer transition times are different for corrugated and isotropic random surface. Hence, connectivity between inner and outer transition times can be used to differentiate between them. Results are obtained under various charge transfer conditions such as diffusion limited,[7,8] reversible[8] and quasireversible cases. It is important to point out that inverse problem under the quasireversible charge transfer has the advantage of tuning the roughness measurement time by adjusting the surface potential.

4. Two other sources of complexity arising in the analysis of electrochemical interfaces are:

(*i*) *the nonlinear dependence of the electron transfer current on the potential difference*: We invert the nonlinear current-potential relationship in the form of power series appropriate to the two extremes, namely, near reversible and near irreversible using the Lagrange or the Ramanujan methods. Transforming both into the Padé expressions, we construct the potential-time profile by retaining whichever is the more accurate of the two[12].

(*ii*) *the coupling of electron transfer with several homogeneous reactions* with attendant diffusion of the species involved. This problem for expanding plane model for DME and planar electrode are handled using systems formalism[12,13]. The interfacial concentration transients obtained here pertain to arbitrary homogeneous reaction schemes coupled to the oxidant and reductant of a single charge transfer step. For the expanding plane electrode model for DME the power-law current form with and without a preceding blank period are analysed.

References

1. VETTER, K. J. *Z. Phys. Chem.*, 1952, **199**, 300.
2. DE LEVIE, R. *Electrochim. Acta*, 1965, **10**, 113.
3. DE LEVIE, R. Electrochemical response of porous and rough electrode. In *Adv. Electrochem. Engng.*, 1967, Vol. 6, p. 329.
4. NYIKOS, L. AND PAJKOSSY, T. *Electrochim. Acta*, 1990, **35**, 1567, and references therein.
5. DE LEVIE, R. *J. Electroanal. Chem.*, 1990, **281**, 1, and references therein.
6. PAJKOSSY, T. *J. Electroanal. Chem.*, 1991, **300**, 1 and references therein.
7. KANT, R. *Phys. Rev. Lett.*, 1993, **70**, 4094.
8. KANT, R. *J. Phys. Chem.*, 1994, **98**, 1663.
9. KANT, R. AND RANGARAJAN, S. K. *J. Electroanal. Chem.*, 1994, **368**, 1.
10. BALIAN, R. AND BLOCH, C. *Ann. Phys.*, 1970, **60**, 401; 1974, **84**, 559.
11. DUPLANTIER, B. *Physica A*, 1990, **168**, 179.
12. KANT, R. AND RANGARAJAN, S. K. *J. Electroanal. Chem.*, 1990, **277**, 19.
13. KANT, R. AND RANGARAJAN, S. K. *J. Electroanal. Chem.*, 1989, **265**, 39.

Thesis Abstract (Ph. D.)

Magnetism and exchange in the layered transition metal thiophosphate and their solid solutions by Nirmala Chandrasekharan

Research supervisor: S. Vasudevan

Department: Inorganic and Physical Chemistry

1. Introduction

The transition metal thiophosphates, MPS_3 (M = Mn, Fe, Ni), are one of the few layered systems in which both the magnetic and crystallographic lattices are two dimensional. In these compounds the layers are separated by van der Waals gaps and as a consequence, they may be intercalated by a wide variety of guest molecules or ions. The metal–ligand interactions are ionic[1] and synthesis of solid solutions of the formula $M'_{1-x}M_xPS_3$ (M', M = Mn, Fe, Ni, Zn) may be anticipated over the entire concentration range.

The objective of the work was: (i) to obtain an adequate description of magnetism in the host MPS_3 (M = Mn, Fe, Ni), and (ii) to try and prepare host lattices with different magnetic properties by forming solid solutions of the formula $M'_{1-x}M_xPS_3$ (M', M = Mn, Fe, Ni, Zn); if successful, the lattice may provide interesting systems for future studies in intercalation reactions.

2. Experimental

The MPS_3 and their solid solutions, $M'_{1-x}M_xPS_3$ were synthesised from their respective elements and single crystals grown by chemical vapour transport. They were characterised by X-ray diffraction and elemental analysis. Homogenous solid solutions obeying Vegard's law were found to form over the entire concentration range.

Temperature-dependent magnetic susceptibility measurements of the powder samples and crystals were performed in an automated Faraday balance (Cahn 2000). Measurements in the temperature range 30–300 K were performed using a closed-cycle cryostat (Air Products). The susceptibility measurements in the temperature range 300–650 K were performed using a high-temperature furnace assembly.

3. Magnetism in transition metal thiophosphates, MPS_3

Transition metal thiophosphates order antiferromagnetically at low temperatures. Their magnetic behaviour is influenced by two important factors, namely, (i) the two-dimensional (2-D) character of the magnetic interactions which include both direct and superexchange, and (ii) the trigonal distortion of the MS_6 octahedra; the trigonal distortion axis being perpendicular to the layer. The 2-D nature of magnetism is a direct consequence of the layered nature of the MPS_3 structure. A consequence of the two-dimensionality of the lattice is that short-range spin correlations manifest at temperatures much higher than the Neel temperature[2]. Hence, any model used to describe the paramagnetic susceptibility would have to account for the 2-D nature of the lattice and the short-range correlations. The trigonal distortion of the MS_6 octahedra in combination with the spin–orbit coupling introduce anisotropy in an otherwise isotropic situation The anisotropy in the magnetic susceptibilities in these systems arises from purely crystal field effects, rather than anisotropic exchange.

The anisotropic magnetic susceptibilities of the layered antiferromagnet $NiPS_3$ (T_N = 155 K) were measured between 30 and 675 K. The susceptibilities showed a weak XY anisotropy in the high-temperature paramagnetic phase with $\chi_\perp > \chi_\parallel$, where $\chi_\parallel$ is the susceptibility when the external field is along the trigonal axis ($\perp$ to the layer). The system may be described by the effective spin Hamiltonian $\mathcal{H} = DS_{iz}^2 - \sum_{ij} J_{ij}\vec{S}_i.\vec{S}_j$. with the quadratic single-ion anisotropy terms introducing anisotropy in an otherwise isotropic situation. The exchange J and single-ion anisotropy parameter D were determined from an analysis of the high-temperature anisotropic susceptibility data. Two approaches have been explored: (i) the method of Oguchi[3] which treats a pair of spins exactly while their interaction with the rest of the crystal is represented by a mean field, and (ii) an adaptation of the correlated effective field theory of Lines[4] in which the mean field felt by an ion is treated as a sum of an ensemble average of the rest of the spins and a term proportional to the instantaneous deviation of the spin of the ion from its average value. Expressions for the anisotropic susceptibilities have been derived for the two models and exchange and crystal field parameters evaluated by fitting to the experimental data. It was found that CEF approximation was superior to the Oguchi model in being able to account for short-range antiferromagnetic correlations and hence gave a better description of the susceptibility in $NiPS_3$. The exchange and crystal-field parameters for the CEF approximation were $J/k = -58.0$ K; $D/k = 16.1$ K; $g_\parallel = 2.05$ and $g_\perp = 2.13$.

The accuracy of CEF approximation was also ascertained by comparing of the calculated susceptibilities in CEF with the experimental susceptibility of the isotropic Heisenberg-layered antiferromagnet $MnPS_3$ for which the high-temperature series expansion susceptibility is available[5]. The comparison also establishes the effectiveness of the special k point scheme[6] in providing Brillouin zone averages in the computation of susceptibilities in the CEF approximation.

The anisotropic magnetic susceptibility of the two-dimensional orbitally unquenched Ising antiferromagnet $FePS_3$ was analysed in the CEF approximation. The formalism introduces spin

correlations in the simplest possible manner while at the same time accounting for the excited states of the orbitally unquenched transition metal ion, the energies of which are comparable to exchange and thermal energies. In $FePS_3$ the degeneracy of the $^5\Gamma_2$ state is completely lifted by the combination of trigonal distortion of the FeS_6 octahedra, spin-orbit coupling and Zeeman splitting. In the calculation of the susceptibilities in the CEF approximation the entire 15-level structure of the $^5\Gamma_2$ state was retained. Good agreement with experiment was obtained for $\Delta/k = 215.5$ K; $|\lambda|/k = 166.5$ K; $J_{nn}/k = 27.7$ K; and $J_{nnn}/k = -2.3$ K. Using these values of the crystal field and exchange parameters, the CEF predicted a $T_N = 123$ K for $FePS_3$ which was identical to the observed value of T_N.

4. Magnetism in the zinc-diluted transition metal thiophosphates, $Zn_{1-x}M_xPS_3$

Before tackling these complicated multicomponent systems in which M′ and M have different energy-level structures, simpler diamagnetically diluted MPS_3 compounds of the formula $Zn_{1-x}M_xPS_3$ were investigated. The powder susceptibilities of the $Zn_{1-x}M_xPS_3$ were measured over the entire concentration range between 30 and 300 K. Transitions were observed below the percolation threshold ($x = 0.7$) for nearest neighbour interactions for a honeycomb lattice. The plots of the molar Curie constant C_m *vs* concentration x showed a linear variation. Crystals of some of the compositions were obtained and the anisotropic magnetic susceptibilities reported between 30 and 300 K.

An adequate description of magnetism in the diluted phases was obtained in the framework of CEF for the high-temperature regime. The validity of the extended CEF formalism was ascertained by noting that the exchange and crystal field parameters did not change on dilution; hence, in these calculations there were no variable parameters. x was determined by AAS. The calculated susceptibilities compared very favourably with experimental data, especially below the percolation threshold. The calculated anisotropic magnetic susceptibilities were also good compared to the experimental susceptibilities in case of crystals. The decrease in anisotropy for low concentrations of the magnetic ion agreed extremely well with those obtained from CEF.

5. Magnetism in the mixed transition metal thiophosphates, $M'_{1-x}M_xPS_3$

Magnetic susceptibility measurements in the temperature range 30–350 K were performed on the powders and a few crystal compositions. The CEF was further developed to account for magnetism in the mixed metal thiophosphates. The crystal field parameters were maintained the same as in the end members of the series, since the local environment around the magnetic ion was not expected to undergo any significant distortion. x was obtained from AAS measurements. The only floating variable was $J_{M-M'} = J_{M-M''}$.

It was found to be 2.0 K for J_{Ni-Fe} throughout the range of x. Neutron diffraction has determined the magnetic ordering in $NiPS_3$ and $FePS_3$ to be the same. From the results of the fit and of a plot of T_N *vs* x (or the predicted trends in T_N obtained from T_{max} *vs* x) a single type of magnetic ordering was predicted throughout the concentration range for $Fe_{1-x}Ni_xPS_3$. In the case of $Mn_{1-x}Ni_xPS_3$, the fits obtained were good for the high-temperature paramagnetic regime for a value of $J_{Ni-Mn} = -26$ K. As in the former case, a single type of magnetic ordering was proposed on the basis of the fit and the plot of T_N *vs* x. For $Mn_{1-x}Ni_xPS_3$, good fits were obtained for $J_{Fe-Mn} = 0.7$ K for the iron-rich phases and $J_{Fe-Mn} = -2.0$ K for the manganese-rich phases. Neutron-diffraction results show that the extreme members of this series, $FePS_3$ and $MnPS_3$, have different types of magnetic ordering. The predicted trends in T_N *vs* x reveal a tetracritical point in the

composition range $0.7 > x > 0.3$. The phase diagram so obtained has been attributed to competing magnetic ordering.

References

1. JOY, P. A. AND VASUDEVAN, S. *Phys. Rev. B*, 1992, **46**, 5134.
2. DE JONGH, L. J. AND MIEDEMA, A. R. *Adv. Phys.*, 1974, **23**, 1.
3. SMART, J. S. *Effective field theories of magnetism*, 1966, W. B. Saunders.
4. LINES, M. E. *Phys. Rev. B*, 1974, **9**, 3927.
5. JOY, P. A. AND VASUDEVAN, S. *Phys Rev. B*, 1992, **46**, 5425.
6. CUNNINGHAM, S. L. *Phys. Rev. B*, 1974, **10**, 4988. [The wavevectors (in unit of π/a) for the 2-D hexagonal lattice along with the weightage factors are (2/9, 2/9t), 1/9; (4/9, 4/9t), 1/9; (8/9, 8/9t),1/9; (2/3, 2/9t), 2/9; (8/9, 4/9t), 2/9; (10/9, 2/9t), 2/9. $t = \sqrt{3}$]

Thesis Abstract (Ph. D.)

Studies on the synthesis, structure and reactivity of polynuclear copper complexes

by N. Vijayashree
Research supervisor: A. G. Samuelson
Department: Inorganic and Physical Chemistry

1. Introduction

The study of synthesis, structure and reactivity of polynuclear metal complexes has received considerable attention in the past 20 years due to the following reasons. One is the proposition that polynuclear metal complexes with metal–metal bonds (metal clusters) could be good chemical models for chemisorption and catalytic reactions occurring on a metal surface[1]. Another is the possibility of mimicking enzymes[2]. The third is the hope that a number of these polynuclear complexes may offer new possibilities for activating organic and inorganic molecules by a cooperative involvement of their metal centres[3]. A number of examples are known in literature in which the polynuclear metal complexes bring about reactions that are either difficult or impossible at a single metal centre and stabilize reactive intermediates by multimetal interaction[4]. The interest in polynuclear copper complexes is due to their ability to activate molecular oxygen. Polynuclear copper complexes serve as models for copper proteins[5] and as catalysts for the oxidation of organic substrates by molecular oxygen[6]. The present investigation is concerned with the possible cooperativity among metal centres in polynuclear copper complexes while activating organic and inorganic substrates. To this end, polynuclear copper (I) complexes of the general formula $[Cu_x(\text{diphosphine})_y(CH_3CN)_z](ClO_4)_x$, where diphosphine was either dppe(1,2-bis(diphenylphosphino)ethane) or dppm(bis(diphenylphosphino)methane) were prepared. Their structures in solid state and in solution were deduced using analytical, spectroscopic, and X-ray diffraction techniques. The reactions of these complexes were carried out with substrates such as allylic halides, organic vicinal and geminal dihalides, sulfur, sodium sulfide, carbon disulfide, dithiocarbonates, aryloxides and phenyl acetylene. In suitable cases, the reactivity of these polynuclear complexes was compared with that of mononuclear complexes.

Table I
Complexes prepared from $[Cu(CH_3CN)_4]ClO_4$ and dppe/dppm

Complex	Formula	Complex	Formula
1	$[Cu_2(dppe)\ (CH_3CN)_6]\ (ClO_4)_2$	6	$[Cu_2(dppm)\ (CH_3CN)_5]\ (ClO_4)_2$
2	$[Cu_2(dppe)_2\ (CH_3CN)_7]\ (ClO_4)_3$	7	$[Cu_3(dppm)_2\ (CH_3CN)_5]\ (ClO_4)_3$
3	$[Cu_2(dppe)_2\ (CH_3CN)_2]\ (ClO_4)_2$	8	$[Cu_4(dppm)_3\ (CH_3CN)_6]\ (ClO_4)_4$
4	$[Cu_2(dppe)_3\ (CH_3CN)_2]\ (ClO_4)_2$	9	$[Cu_2(dppm)_2\ (CH_3CN)_2]\ (ClO_4)_2$
5	$[Cu_3(dppe)_4\ (CH_3CN)_2]\ (ClO_4)_3$	10	$[Cu_2(dppm)_3\ (CH_2CN)_2]\ (ClO_4)_2$

Complexes 9 and 10 were prepared according to literature procedures.

2. Results

The complexes prepared in the present study are listed in Table I.

The dppm in these complexes was only bridging. Cu(I)-dppm complexes did not dissociate in solution. The chemistry of Cu(I)-dppe complexes was more complex as dppe was either bridging or chelating or both depending on the ratio(mol) of Cu(I) to dppe. Complexes 1 and 2 with Cu(I)/dppe>1 contained bridging dppe and retained their structure in acetone and methylene chloride solutions (*vide* proton and phosphorus-31 NMR spectroscopy). However, these complexes dissociated to form free $[Cu(CH_3CN)_4](C1O_4)$, when acetonitrile was used as the solvent for spectroscopy. Complex 4 with Cu/dppe<1 had chelating and bridging dppe in the solid state and in solution. Complex **3** with Cu(I)/dppe = 1 was unique in that it contained bridging dppe in the solid state but underwent dissociation in solution-forming complexes with chelating dppe. Variable temperature ^{31}P NMR studies on complexes **3** and 4 shed light on the different species that are present in solution.

Crystallographic studies on complex **3** revealed the presence of rare, doubly bridging, dppe units. The structure is interesting considering the predominantly chelating nature of dppe and the strain involved in holding two *trans* dppe units across two metal centres.

In the case of complex **1** which could not be crystallised, the solid-state structure was deduced from solid-state CP/MAS ^{31}P NMR spectra. Interestingly, the CP/MAS ^{31}P resonances of complexes in solid state were different from those in solution. The resonance due to bridging dppe in different complexes appeared at the same value in solution. However, in solid state, chemical shifts were determined not only by the bridging or chelating nature of dppe, but also by the conformation adopted by the ligand.

Complexes **1**, **3**, **7** and **10** formed a series of binuclear complexes with different intermetallic distances. The synergistic effect of adjacent metal centres was observed in reactions with allyl halide, cinnamylidene chloride and phenyl actylene. A copper–allyl complex was identified from spectroscopic data in reactions with allyl halides. Under suitable conditions phenyl acetylene units could be oxidatively coupled to form the dimer, as in Glazer coupling.

Based on the reactions with chalcone dibromide, a synthetic procedure for the chemoselective debromination of activated dibromides, using copper powder was developed.

A low-temperature route for the synthesis and interconversions of technologically important copper sulfides was discovered, during the course of attempts to prepare polysulfide complexes of copper.

The oxidation of catechol, phenyl acetylene and 2, 6-dimethylphenol by oxygen was carried out using a hexanuclear copper(II) complex which had been reported to contain a di-μ-oxo-di-

copper(II) core[7], as the catalyst. It was understood from the products obtained that the complex contained a di-μ-hydroxo-di-copper(II) core and not the reported di-μ-oxo-di-copper(II) core.

References

1. MUETTERTIES, E. L. *Science*, 1977, **196**, 839.
2. SORRELL, T. N. *Tetrahedron*, 1989, **45**, 3.
3. WERNER, H. *Comments Inorg. Chem.*, 1990, **10**, 267.
4. WILKE, G. *Pure. Appl. Chem.*, 1978, **50**, 677.
5. CASELLA, L. *et al.* *Inorg. Chem*, 1993, **32**, 2056.
6. GAMPP, H. AND ZUBERBUHLER, A. D. *Metal Ions Biol. Systems*, 1981, **12**, 133.
7. MATHEWS, I. I. *Investigations on the reactions of Vitamin B_6 in model systems. Synthesis and structural studies on metal complexes of Vitamin B_6-related compounds*, Ph. D. Thesis, Indian Institute of Science, Bangalore 1991.

Thesis Abstract (Ph. D.)

First order hyperpolarizability–structure relationship in donor–acceptor substituted ethylenes and 1,3-butadienes by K. Mohanalingam

Research supervisor: P. K. Das

Department: Inorganic and Physical Chemistry

1. Introduction

The progress in photonic devices requires the development of novel materials exhibiting strong optical nonlinearities both at the molecular level and in the bulk[1–3]. The overall objective of this work is to arrive at structure–property relationships in substituted ethylenes and 1,3-butadienes (conjugated organic systems) leading to large second-order nonlinearities as measured by their second harmonic generation (SHG) coefficients in solution and efficiency in the bulk.

2. Synthesis

Various monoamino-substituted nitroethylenes were synthesized using modified methods reported in literature. 1-N, N-dimethylamino-2-nitroethylene (**1a**) was synthesized by the condensation of N, N-dimethylamino-O, O-dimethylacetal and nitromethane at 70°C. The other nitroenamines, namely, 1-pyrrolidino (**1b**), 1-piperidino (**1c**), 1-morpholino (**1d**) and 1-prolinato (**1e**)-substituted nitroethylenes were synthesized by replacing dimethylamino group in (**1a**) with respective amines. The nitroenamines studied and the general reaction scheme for their synthesis are given in Fig. 1. 1,1-bisamino-2-nitroethylenes were synthesized by the replacement of alkylthio groups from 1,1-bis(methylthio)-2-nitroethylene (**2a**) with the corresponding amino groups. Molecular and crystal engineering approaches to produce noncentrosymmetric structures have been used[4]. The compounds synthesized using this method were obtained by the replacement of methylthio groups from compound **2a** with N-methylamine (**2b**), N, N-dimethylamine (**2c**) and α-methylbenzylamine (**2d**) in the presence of *p*-toluenesulfonic acid as catalyst and the compounds studied are given in Fig. 2. In order to study the chain length dependence of the first-order hyperpolarizability, in simple polyenes a series of substituted 1,3-butadienes have been made. The reaction scheme used for the synthesis of these compounds is given in Fig. 3.

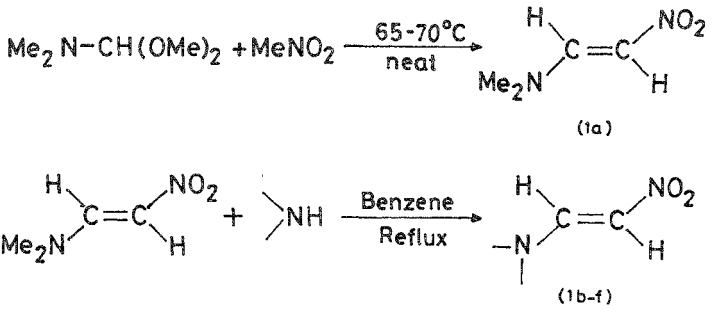

FIG. 1.

3. Measurement techniques

The powder second harmonic generation efficiency and charge transfer contribution to the first-order hyperpolarizability, β_{CT} of all the nitroenamines synthesized were obtained by Kurtz's pow-

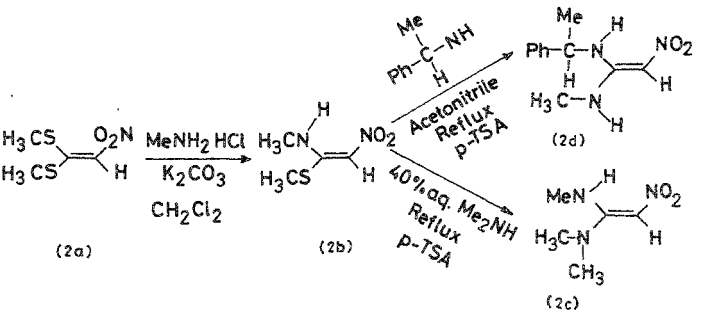

FIG. 2.

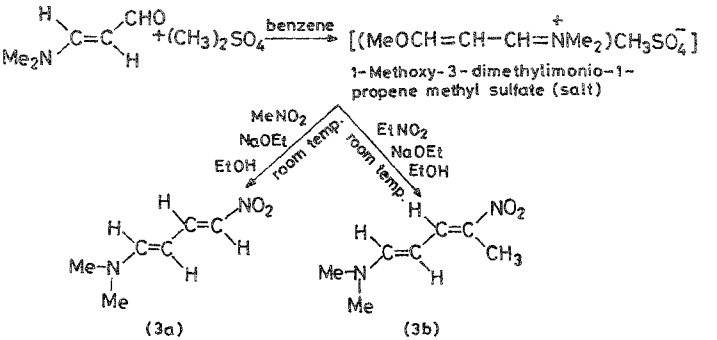

FIG. 3.

der technique and a two-level model, respectively. The experimental set-up used for the study of SHG efficiency is given in Fig. 4.

The expression used in the two-level model for obtaining β_{CT} is given by

$$\beta_{CT} = 3e^2\hbar^2 Wf\Delta\mu_{g-e}/2m[W^2-(2\hbar\omega)^2][W^2-(\hbar\omega)^2]$$

where the change in dipole moment $\Delta\mu_{g-e}$ was obtained from known values or theoreticals estimates of μ_g through semi-empirical MNDO or AM1 methods, the solvent-induced absorption spectral shifts and the oscillator strength obtained from the absorption spectrum of the compound. The nitroenamines investigated show large bathochromic shifts in their absorption band when the solvent polarity was increased. This is due to greater stabilization of these enamines in polar solvents in excited state compared to the ground state.

In the simple nitroenamines (**1a–e**), none of the compounds exhibited measurable second harmonic generation in the powder form[5], although all the compounds were having large β_{CT} values. The introduction of the second electron-donating group as expected showed an altered elec-

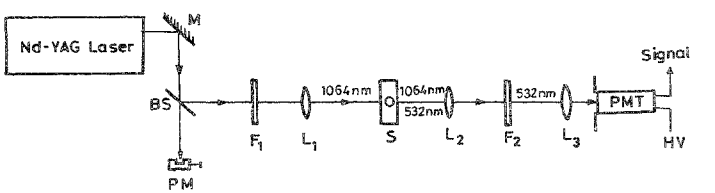

L_1, L_2, L_3: Lenses, M: 99% Reflecting mirror, PM: Powder meter, BS: 50% Beam splitter, S: Sample holder, F_1, F_2: Filters (KG-5 AND $CuSO_4$), PMT: Photo multiplier tube, HV: DC High volyage.

FIG. 4.

tronic charge distribution and an increased steric crowding resulting in a decrease in the magnitude of β_{CT}. The 1,1-bispiperidino-2-nitroethylene was not only found to have the highest first-order hyperpolarizability in the series, but it also showed SHG intensity. The other compounds did not exhibit any measurable SHG intensity. The crystal structure of the above compound that exhibited SHG was determined and the compound crystallizes in a noncentrosymmetric structure. The compound crystallized in the $P2_12_12_1$ space group with four molecules in the unit cell. One of the interesting aspects about the structure is the elongated C = C bond distance (1.40 Å) which points out extensive charge delocalization in the molecule. In spite of having a noncentric structure, the orientation and packing of the molecules in the unit cell were found to be unfavourable for the compound to exhibit very large SHG. This is explained by the unfavourable angle between the CT axis of the molecule and the crystallographic axes within the oriented rigid gas approximation. The CT axis makes an angle of 73.2, 36.6 and 58.5° with the crystallographic a, b and c axes, respectively.

Introduction of chiral and hydrogen bonding group is expected to play a role in orienting the molecules 'properly' and hence improve the packing characteristics (**2a–d**). Although the β_{CT} values obtained for these were not very different from the compounds discussed earlier, the compound having the electron donors methylamino- and α-methylbenzylamino groups (with the nitro group as the acceptor) exhibited a measurable second harmonic intensity (0.25 times of that of urea). The crystal structure of the compound was determined and it was found to crystallize in an acentric space group, P21. Both intra- and inter-molecular H-bondings were present in the compound with extensive charge transfer between the donor and the acceptor groups. Application of the oriented rigid gas model to this molecule also explains low SH efficiency in this compound.

In so far as the effect of increasing the chain length of the π system on β is concerned only in 1-N,N-dimethylamino-4,4-dicyano-1,3-butadiene there was an enhancement in β compared to that of the similarly substituted ethylene. However, none of the butadiene compounds produced detectable SH intensity. In order to understand the second-order nonlinearities in these systems, the crystal structure of 1-N,N-dimethylamino-4,4-bis(trifluoroacetyl)-1,3-butadiene was determined and it crystallizes in a centric space group (P1). The observed bond lengths and angles in this compound indicate the presence of extensive delocalization of electrons between the donor and acceptor groups.

In conclusion, substitution of hydrogens in ethylene by donor and acceptor groups leads to a large ground-state dipole moment because of which the molecules tend to form psuedo-inversion dimers in the crystal lattice. Orientation and packing of molecules in the unit cell are very crucial for exhibiting very large second-order nonlinearities. In the simple nitroenamines studied the β_{CT} values obtained correlate with $\Delta\mu_{g-e}$ as predicted by the two-level model. A similar trend is also observed in the 1,1-bisaminonitroethylenes. However, the observed β values of the bisamino séries is about three times less compared to monoamino-substituted nitroethylenes. This decrease is associated with increased steric interactions between the donor and the acceptor groups. Among the compounds possessing hydrogen bonding and chiral center as part of the electron-donating group, 1-N-methylamino-1-α-methylamino-2-nitroethylene shows maximum SH intensity. This is attributed to the combined electronic and steric factors. Although H-bonding helps molecules overcome the dipolar attraction forces, its role in maximizing SHG and β is not very clear. The scaling of β_{CT} in N,N-dimethylamino and cyano-substituted polyenes follows an L^{27} (where L is the length of the molecule) behaviour which agrees well with a π-electron exact model for calculating β.

References

1. ZYSS, J. AND CHEMLA, D. S. (EDS) *Nonlinear optical properties of organic molecules and crystals*, Vols. 1 and 2, 1987, Academic Press.
2. STUCKY, G. D., MARDER, S. R. AND SOHN, J. E. (EDS) *Materials for nonlinear optics: A chemical perspective*, ACS Symposium Series 455, ACS, Washington DC, 1991.
3. PRASAD, P. N. AND WILLIAMS, D. J. *Introduction to nonlinear optical effects in molecules and polymers*, 1991, Wiley.
4. MOHANALINGAM, K., DAS, P K. AND RAJAPPA, S. *Spectrochim. Acta A*, 1992, **48**, 1647–1656.
5. MOHANALINGAM, K. AND DAS, P. K. *Indian J. Chem. A*, 1992, **31**, 518–525.

Thesis Abstract (Ph. D.)

Molecular dynamics studies of structure and transport in some inorganic glasses by S. Balasubramanian

Research supervisor: K. J. Rao

Department: Solid State and Structural Chemistry Unit

1. Introduction

Amorphous materials, particularly glasses, have been known for a long time but they are less understood than crystalline materials[1]. This is largely due to the absence of periodicity in amorphous substances. An important feature of glasses is the existence of short-range order which is often, if not universally, similar to that in the corresponding crystal. Glasses span a wide range of conductivity and exhibit both purely electronic as well as ionic contributions. Thus, a study of the structural and transport properties of inorganic glasses is important. Computer simulation techniques in general, and molecular dynamics (MD), in particular, have been employed quite successfully in understanding the structure and dynamics of liquids and glasses[2]. Through MD, it is fairly straightforward to obtain partial pair correlation functions through simulations unlike in diffraction experiments, where only the total radial distribution function is obtained. Apart from static structure, MD can also provide rich details on the microscopic dynamics and transport of the various species in the system, which can serve as a complementary tool to interpret inelastic neutron scattering data. It should however be cautioned that the results obtained from a simulation can mimic the real system well only if accurate potentials are employed. Due to the complexity of the nature of interactions in glasses, every glass system has to be treated specifically.

A survey of the current understanding of the problems in glass science is made in the introduction to the thesis. In particular, various experimental and modelling techniques to study the local and intermediate range order in glasses have been introduced. The concept of random close packing to study largely ionic glasses is reviewed. Though glasses are largely frozen, conductivity relaxations can get decoupled from the structural relaxations, leading to a finite conductivity in the system. Thus transport properties of glasses are also worthwhile to study. The key problems related to transport of ions in glasses, in particular silicates, are presented. The use of molecular dynamics technique to study problems of glasses is discussed and the importance of the potential model in simulations is stressed. The computer-simulated glasses have been known to possess high fictive temperatures due to high-quenching rates employed[2] (around 10^{12} K/s) and a comparison of such glasses with experimentally prepared samples has been made.

2. Results and discussion

We have performed a detailed molecular study of the mixed alkali effect in silicate glasses. Mixed alkali effect has been one of the challenging problems in glass science[3]. To understand the microscopic origin of this effect, an MD study of the effect in (Li, $K)_2O$. SiO_2 glass has been performed using the Born–Mayer–Huggins potential. In the present study, subtle structural variations in the local environment of alkali ions are observed as a function of (Li/K) ratio. Mixed alkali effect has been observed in the variation of self-diffusion coefficients and thus in electrical conductivity. Cage vibration frequencies of the alkali ions remain unaffected as a function of interalkali concentration, contrary to the expectation of electrodynamic approaches like the Hendrickson and Bray model. van Hove correlation functions (which are both space and time dependent) have been employed to study the nature of transport process of the alkali ions. Results indicate that alkali ions preferentially jump only to like ion sites[4] at low temperatures which has been rationalized in terms of their site energies. This observation resolves quite satisfactorily the origin of mixed alkali effect.

The temperature dependence of the migration of alkali ions and the detailed nature of their paths in potassium disilicate glass have also been investigated. The potential model proposed by Tsuneyuki *et al.*[5] has been employed with suitable modifications. The nature of the potential enables the use of partial charges and thus the identification of bridging (BO) and nonbridging oxygens (NBO), based directly on their charges and not through any distance criterion. In the present study, potassium ions are found to be octahedrally coordinated to oxygen. Again, using van Hove correlation functions it is shown that the motion is essentially jump like even up to 1500 K (close to T_g) and becomes diffusive at higher temperatures. Time–temperature complementarity has been observed to be valid in the present simulations. The hops in these glasses occur preferentially to sites rich in NBO coordination, thus supporting the assumption involved in the modified random network model[6] for the existence of conduction pathways. The activation energies for alkali ion jumps obtained under a classical activation picture using jump time distributions and cage vibrational frequencies match well with experiments.

Na_2SO_4–$ZnSO_4$–K_2SO_4 melts form archetypal ionic glasses. Local environment of cations in these glasses in widely varied. This system has been studied by considering the $(SO_4)^{2-}$ units as rigid tetrahedra. It has been observed that while zinc prefers octahedral coordination, sodium is surrounded by 8 oxygens and potassium by nearly 12. Computer simulation results largely support the random close-packing model for these glasses in which $(SO_4)^{2-}$ ions are considered as pseudospherical[7]. The dynamics of the cations and the rotational motion of sulfate tetrahedra are studied and the results of the dynamical data strongly suggest the occurrence of MAE in this glassy system. The cage vibrational frequencies of the cations obtained from their velocity autocorrelation functions are in good agreement with experiments.

While MD of ionic systems has developed considerably, very little work has been done on covalent materials. The *ab-initio* methods developed recently attempt to solve some of the difficulties involved in the simulation of such systems. Yet, it is possible to stimulate the covalent bond in MD formulation by considering groups of atoms within which the interaction is particularly strong and localized. The simulation of some glasses with largely covalent interactions is presented in Part II of the thesis. One such case is glassy selenium, which is known to exist in the form of chains. Thus in the present MD simulation of g-Se presented in Section 1, 10 chains of 30 atoms each were considered to be representative model of the system. A harmonic potential was employed for nearest neighbour interactions, while intra- and interchain interactions were modelled by the Lennard–Jones form. The model provides good agreement with experimental pair

correlation functions[8] and bond-angle distributions. The dihedral angle distribution does not exhibit any preference, possibly due to free rotation allowed in potential form. Diffusion coefficient obtained from the study indicates localised motion of the chains as is observed in inelastic neutron scattering experiments.

A study in the same spirit was undertaken on the MD simulation of g-B_2S_3. This is the base glass of the superionic conductor LiI–Li_2S-B_2S_3. Hence, a structural study of this glass is essential to understand its role in the conduction of Li^+ ions. In addition, sulfur-containing glasses are known to form edge-shared units unlike oxygen-containing glasses in which corner-sharing is preferred. The interactions in B_2S_3 are largely covalent and hence in addition to pairwise interactions, three-body forces were specifically introduced to reproduce the strongly directional nature of the bonding. All the interatomic distances in the glass are well reproduced and B_2S_3 glass has been shown to have a chain-like structure with planar B_2S_2 rings alternating between any two sulfur atoms in good agreement with experiments[9]. The first peak in the neutron structure factor, $S_n(q)$ at 1.4 $Å^{-1}$ is observed in the simulations and an analysis of the various features in $S_n(q)$ is made. The first peak has been found to signify cation–cation spatial correlations at around 5.6 Å implying intermediate range order in these glasses. The first peak is likely to be of the nature of the first sharp diffraction peak (FSDP) observed in many network glasses. Computer-simulated systems have been known to show a higher glass transition temperature due to the high rate of quenching. From a study of the Abraham–Wendt ratio and the mean squared displacement data, the glass-transition temperature of the computer-simulated system has been found to be around 800 K in comparison to around 480 K obtained from differential scanning calorimetric measurements.

The molecular dynamics method, its application to the study of glasses and the various correlation functions employed to analyse the results obtained from simulations are also presented.

References

1. RAO, K. J. AND SHASTRY, M. C. R. — In *Chemistry of advanced materials* (C. N. R. Rao, ed.) IUPAC monograph, pp. 369–382, 1993, Blackwell.
2. ANGELL, C. A., CLARKE, J. H. R. AND WOODCOCK, L. V. — *Adv. Chem. Phys.*, 1981, **48**, 397–453.
3. INGRAM, M. D. — *Phys. Chem. Glasses*, 1987, **28**, 215–234.
4. MAASS, P., BUNDE, A. AND INGRAM, M. D. — *Phys. Rev. Lett.*, 1992, **68**, 3064–3067.
5. TSUNEYUKI, S., TSUKADA, M., AOKI, H. AND MATSUI, Y. — *Phys Rev Lett.*, 1988, **61**, 869–872.
6. GREAVES, G. N. — *Phil. Mag. B*, 1989, **60**, 793–800.
7. SUNDAR, H. G. K. AND RAO, K. J. — *J. Chem. Soc. Faraday Trans. I*, 1980, **76**, 1617–1629.
8. HANSEN, F. Y., KNUDSEN, T. S. AND CARNEIRO, K. — *J. Chem. Phys.*, 1975, **62**, 1556–1565.
9. MENETRIER, M., HOJJAJI, A., LEVASSEUR, A., COUZI, M. AND RAO, K. J. — *Phys. Chem. Glasses*, 1992, **33**, 222–227.

Thesis Abstract (Ph. D.)

Utility of microbes in organic synthesis: (i) Selective transformations of acyclic terpenes, and (ii) Purification and characterization of a novel secondary alcohol dehydrogenase by T. L. Gururaja

Research supervisor: K. M. Madyastha

Department: Organic Chemistry

1. Introduction

Exploration of microbes in carrying out transformations of natural products has been an important and fascinating method in synthetic organic chemistry[1]. It is now becoming widely appreciated that, compared with chemical methods, reactions catalysed by microbes often offer significant advantages including those of efficiency, regiospecificity, stereoselectivity, etc. The conditions under which microbial reactions take place are mild and hence compounds which are sensitive to heat, acid and base become amenable to such transformations. Thus, microbes serve as an important tool in the hands of organic chemists to achieve selective transformations of complex natural products.

Considerable progress has been made in the microbial transformations of various classes of organic compounds[2] such as steroids, carbohydrates and aromatic compounds. Although acyclic terpenes are one of the widely distributed class of natural products, progress in the field of microbial transformations of these compounds lagged behind considerably as compared to other classes of compounds. This is partly due to their antimicrobial nature and due to experimental difficulties involved in working with these volatile substrates.

The objectives of the present investigation were: (i) to find a suitable fungal system for carrying out selective oxidation of various acyclic isoprenoids and to investigate the enzyme system(s) involved in the transformation. (ii) to explore the possibility of transforming acyclic terpenes by

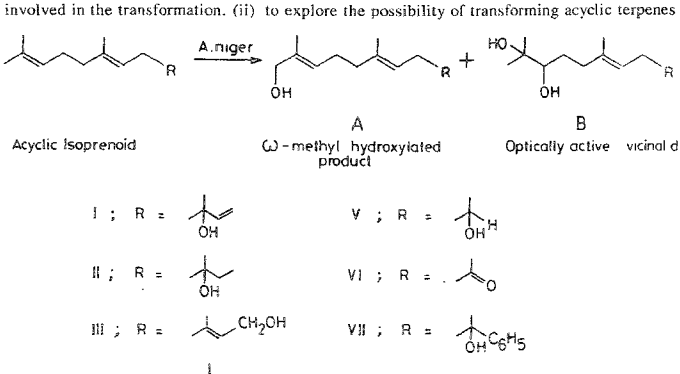

FIG. 1. Selective oxidation of various acyclic isoprenoids by *Aspergillus niger*.

microbial means into useful intermediates and to study some of the properties of the corresponding enzyme after purification.

2. Results and discussion

Earlier we have isolated a strain of *Aspergillus niger* from garden soil which was found to carry out regiospecific ω-methyl hydroxylation of acyclic monoterpene alcohols[3]. Since ω-methyl hydroxylation is one of the important reactions in organic synthesis, we explored the potential of this fungal system to effect such a selective transformation in the case of higher acyclic isoprenoids. To ascertain the versatility and specificity of the organism, we have subjected nerolidol, farnesol and several synthetically modified acyclic isoprenoids (I–VII) to bio-oxidation using *Aspergillus niger*.

When higher acyclic isoprenoids were used as substrates, the organism showed its unique ability to carry out the oxidation of not only the ω-methyl group but also the remote double bond (Fig. 1). However, these two activities appear to have preferential structural requirements, and the ratio of the products formed depends upon the nature of the R-group. Oxidation of the remote double bond in compounds I to VII resulted in the formation of optically active vicinal diols (IB to VIIB). Besides, the organism also carried out asymmetric reduction of VI to optically active V. In the case of III small amounts of IB was also isolated whereas VI gave minor amounts of VA and VB in addition to the other hydroxylated products[4,5].

As compared to the extensive work accomplished in the field of microbial transformations of monoterpenes, only limited data are available on the microbial metabolism of sesquiterpenes. Most of the reports in the literature show that the sesquiterpenes as a group yield relatively fewer

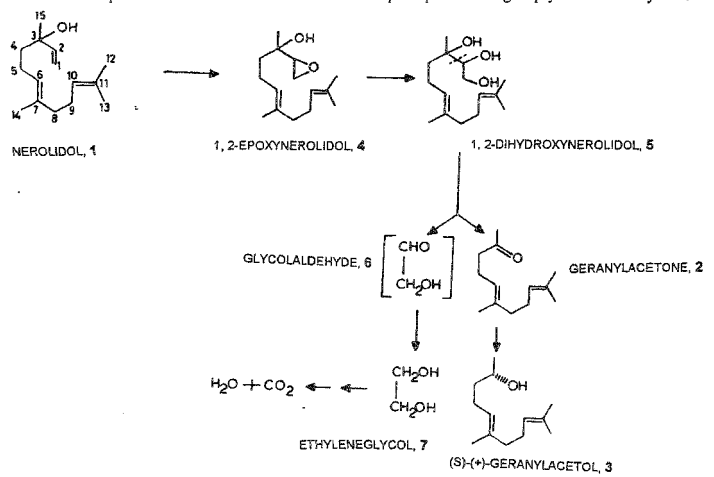

FIG. 2. Proposed pathway for the degradation of nerolidol by *Alcaligenes eutrophus*.

products than the monoterpenes[6]. While this factor ought to have made the study of their microbial metabolism easier, the problem of getting an organism to grow on the sesquiterpene substrate seems to be a major deterrent. Hence, in the present investigation, the study of bacterial metabolism of acyclic sesquiterpene alcohol nerolidol was undertaken.

In an attempt to isolate an organism which can grow on nerolidol as sole source of carbon and energy, a bacterial strain identified as *Alcaligenes eutrophus* was isolated from the garden soil by enrichment culture technique. Degradation of nerolidol (**1**) by *Alcaligenes eutrophus* yielded two major and a couple of very minor metabolites. The major metabolites formed have been identified as geranylacetone (**2**) and optically active alcohol, (S)-(+)-geranylacetol (**3**). On the basis of the metabolites isolated a new pathway for the formation of **3** from **1** was proposed which involves the epoxidation of 1, 2-double bond of **1** to **4** followed by hydrolysis to yield a triol (**5**). Then cleavage of the C_2–C_3 bond leads to the formation of **2** and a glycolaldehyde (**6**). (**2**) and glycolaldehyde (**6**) upon reduction afforded (**3**) and ethyleneglycol (**7**), respectively (Fig. 2). Further support for the proposed pathway comes from the *in-vivo* transformation of synthetically prepared probable intermediates (**4**) and (**5**) to (**2**) and also from the manometric studies which strongly support the postulated pathway[7]. To the best of our knowledge this is the first report on the bacterial degradation of nerolidol.

The cell-free extract (105,000 × g supernatant) prepared from the nerolidol-grown *Alcaligenes eutrophus* converted (**2**) to an optically active alcohol, (**3**) (Fig. 2) in the presence of an external cofactor NAD(P)H demonstrating the presence of an active oxido-reductase[8]. Since asymmetric reduction of prochiral ketones to an optically active alcohol is an important reaction in organic synthesis[9], attention was focussed to purify the enzyme and to study its physico-chemical properties.

An affinity matrix was designed and prepared exclusively for the purification of this particular protein. Secondary alcohol dehydrogenase from *Alcaligenes eutrophus* cell-free extract was purified to homogeneity[10] (using a series of ion exchange and affinity column chromatographies, 5 steps) resulting in 408-fold increase in specific activity. The purified protein gave a single band when examined by SDS-PAGE and the subunit molecular weight was estimated to be 38.5 kDa. It exists in a homotetrameric form under nondenaturing conditions (M_r 139 kDa by gel filtration, FPLC) comprising four identical subunits. The isoelectric point (pI) was determined to be 6.2. NADPH was preferred over NADH. The enzyme catalyses both oxidation and reduction reactions at two different pHs. The optimal pH for the oxidation reaction is 9.5 and for the reduction reaction is 5.5. The reaction was found to be stereospecific. The enzyme exhibited wide-substrate specificity since it accepted various C_{19} steroids besides terpenes. The enzyme has high specific activity for the oxidation of testosterone and K_m for testosterone and $NADP^+$ were 11.76 and 55.56 μM, respectively. The metal-chelating agents and thiol reagents inhibited the protein. The properties of this enzyme were compared with similar enzymes in the current literature, and were found to be significantly different from those thus far described[11–13].

3. Conclusions

To summarise, the present investigation provided a fungal system for carrying out selective oxidation of ω-methyl and remote double bonds of various acyclic isoprenoids. A new pathway for the degradation of nerolidol by *Alcaligenes eutrophus* was documented for the first time and *Alcaligenes eutrophus* grown on nerolidol yielded a pure novel $NAD(P)^+$-linked secondary alcohol dehydrogenase for carrying out asymmetric reduction of various prochiral ketones.

References

1. YAMADA, H. AND SHIMIZU, S. *Angew. Chem. Int. Ed. Engl.*, 1988, **27**, 622–642.
2. GIBSON, D. T. *Microbial degradation of organic compounds*, 1984, Marcel Dekker.
3. MADYASTHA, K. M. AND MURTHY, N. S. R. K. *Tetrahedron Lett.*, 1988, **29**, 579–580.
4. MADYASTHA, K. M. AND GURURAJA, T. L. *Appl. Microbiol. Biotechnol.*, 1993, **38**, 738–741.
5. MADYASTHA, K. M. AND GURURAJA, T. L. *Indian J. Chem. B*, 1993, **32**, 609–614.
6. LAMARE, V. AND FURSTOSS, R. *Tetrahedron*, 1990, **46**, 4109–4132.
7. MADYASTHA, K. M. AND GURURAJA, T. L. *Biochem. Biophys. Res. Commun.*, 1993, **193**, 26–31.
8. MADYASTHA, K. M. AND GURURAJA, T. L. *J. Chem. Technol. Biotechnol.*, 1994, **59**, 249–255.
9. JONES, J. B. *Tetrahedron*, 1986, **42**, 3351–3403.
10. MADYASTHA, K. M. AND GURURAJA, T. L. *Biotechnol. Appl. Biochem.*, 1996, **23**, 245–253.
11. TALALAY, P. AND PAYNE, D. W. *J. Biol Chem.*, 1985, **260**, 13648–13655.
12. ASHRAF, W. AND MURRELL, J. C. *Arch. Microbiol.*, 1990, **153**, 163–168.
13. BRITT, A. J., BRUCE, N. C. AND LOWE, C. R. *FEMS Microbiol Lett.*, 1992, **93**, 49–56.

Thesis Abstract (Ph. D.)

X-ray structural investigations towards the design of nonlinear optical organic materials by Parthasarathi Dastidar

Research supervisor: T. N. Guru Row

Department: Organic Chemsitry

1. Introduction

The search for new organic materials with nonlinear efficiency surpassing those existing has been pursued extensively in recent years[1]. The necessary and sufficient conditions to be satisfied for an organic molecule to show SHG are: (i) the occurrence of charge transfer, (ii) extensive delocalization of π-electrons, if present, (iii) a large difference in dipole moment between ground and excited states, (iv) a noncentrosymmetric crystal structure, and (v) a favourable molecular packing in the crystal lattice. Our main goal in the present study was to prepare new materials belonging to this class and to get an insight into the solid-state structure of these materials which may be useful to design future second-generation nonlinear optical (NLO) organic materials.

2. Results and discussion

(i) Push–pull ethylenes and butadienes as NLO materials

X-ray crystallographic studies on a large number of 'push–pull' ethylenes showed the presence of appreciable π-electron delocalization between donor and acceptor groups through the double bond[2]. Therefore, it is expected that molecules belonging to this class will have significant value of molecular hyperpolarizability β, which is the primary requirement for a molecule to show SHG

activity. In an attempt to search for newer organic materials with large SHG activity and to gain further insights into the correlation between SHG activity and molecular packing, a 'push-pull' ethylene with cyano as the acceptor and dioxolane as the donor has been synthesized (Scheme 1).

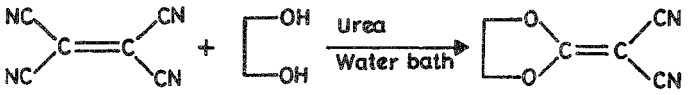

SCHEME 1.

X-ray crystal structure of 2-dicyanomethylene-1, 3-dioxolane (I) and an analysis of the correlation between SHG activity and molecular packing in the crystal lattice have been carried out[3]. Compound (I) crystallizes in a noncentrosymmetric space group Cc ($z = 8$). The charge-transfer-axis of (I), owing to approximate symmetry mm2 of the molecule, passes through the ethylenic double bond and makes an angle of 28.4° with the crystallographic b-axis. This value differs significantly from the theoretically expected value of 54.74° for maximum SHG activity[4]. Also, the occurrence of two molecules in the asymmetric unit and the presence of noncrystallographic 2-fold axis along the a-direction between these two molecules cause compound (I) to show SHG activity only half that of urea.

The molecular hyperpolarizability β of 'push–pull' butadiene would be larger than that of 'push–pull' ethylene because the separation distance of the dipole in 'push–pull' butadiene is much longer than that in 'push–pull' ethylene. In fact, β and $\Delta\mu$ are directly proportional to each other. Therefore, a high value of $\Delta\mu$ of a noncentrosymmetric molecule is enough to ensure a high value of β. Four butadienes of 'push–pull' type (Scheme 2), namely, ethyl 2-cyano-5-

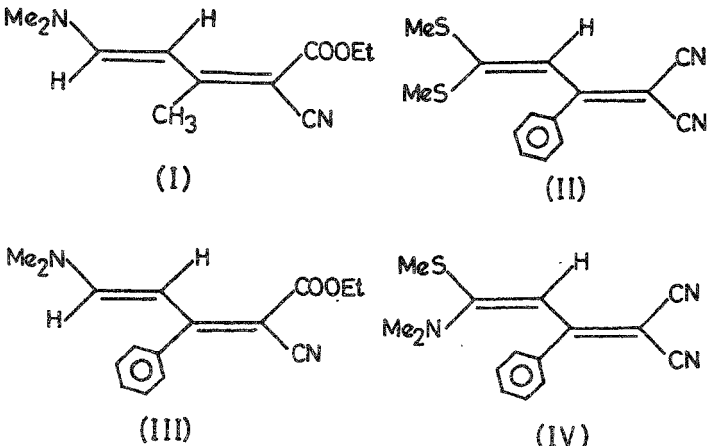

SCHEME 2.

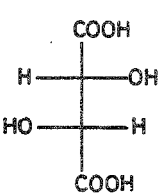

TA

+

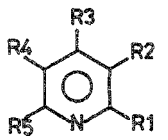

1. R1 = R2 = R4 = R5 = H ; R3 = $-NH_2$
2. R1 = R2 = R4 = R5 = H ; R3 = $-NMe_2$
3. R1 = R2 = R4 = R5 = H ; R3 = $-CH_2-C_6H_4-NO_2$
4. R2 = R3 = R4 = H ; R1 = R5 = $-Me$
5. R2 = R3 = R5 = H ; R1 = $-NH_2$; R4 = $-Cl$
6. 8-Hydroxyquinoline

SCHEME 3.

dimethylamino-3-methyl-2,4-pentadienoate(I), 4,4-bis (methylthio)-2-phenyl-1,3-butadiene-1, 1-dicarbonitrile(II), ethyl 2-cyano-5-dimethylamino-3-phenyl-2,4-pentadienoate(III) and 4-dimethylamino-4-methylthio-3-phenyl-1,3-butadiene-1,1-dicarbonitrile(IV) have been investigated by single-crystal X-ray diffraction studies[5]. All of these crystallize in centrosymmetric space group and therefore do not show any SHG activity. However, detailed analyses of the X-ray results reveal that significant delocalization of π-electrons is present in all these molecules. Theoretical values of β obtained were quite large.

(*ii*) *Hydrogen bond-directed NLO materials*

Large β values do not necessarily ensure excellent SHG activity due to frequent occurrence of centrosymmetric crystals or unfavourable molecular packing in crystal lattice and involves serious

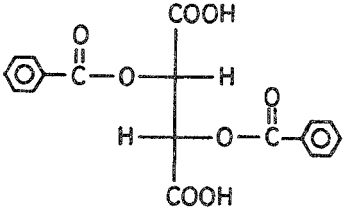

DBT (I)

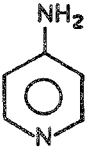

4-AP(II)

SCHEME 4.

synthetic effort. In order to prepare NLO materials in a simple way, a number of hydrogen bond-directed salts of TA and substituted pyridines have been prepared (Scheme 3) and characterised for SHG. One such salt, namely, L-tartaric acid: 4-dimethylaminopyridine (1:1) dihydrate has been subjected to X-ray crystallographic analyses. All these salts have shown SHG activity comparable to that of urea[6].

Attempts to prepare hydrogen bond-directed NLO materials from a 1:1 molar mixture of D-(+)-dibenzoyltartaric acid (DBT) and 4-aminopyridine (4-AP) (Scheme 4) resulted in two salts of different stoichiometry. One of them crystallises in an unusual 1.5:1 (acid:base) monohydrate salt while the other as 1:1 (acid:base) salt. SHG intensity of these salts was found to be 1.4–1.6 times that of urea and both the salts were subjected to X-ray crystallographic analyses[7].

References

1. PRASAD, P. N. AND WILLIAMS, D. J. — *Introduction to nonlinear optical effects in molecules and polymers*, 1990, Wiley.
2. ADHIKESAVALU, D., KAMATH, N. U. AND VENKATESAN, K. — *Proc. Indian Acad. Sci. (Chem. Sci.)*, 1983, **92**, 449.
3. DASTIDAR, P., GURU ROW, T. N. AND VENKATESAN, K. — *J. Mater. Chem.*, 1991, **1**, 1057.
4. ZYSS, J. AND OUDAR, J. L. — *Phys. Rev A*, 1982, **26**, 2028.
5. DASTIDAR, P., GURU ROW, T. N. AND VENKATESAN, K. — *Acta Cryst. B*, 1993, **49**, 900.
6. DASTIDAR, P., GURU ROW, T. N. PRASAD, B. R., SUBRAMANIAN, C. K. AND BHATTACHARYA, S. — *J Chem. Soc. Perkin Trans.* II, 1993, 2419.
7. BHATTACHARYA, S., DASTIDAR, P. AND GURU ROW, T. N. — *Chem. Mater* , 1994, **6**, 53.